Hochschule Aalen

Fakultät Optik und Mechatronik

Master of Photonics

Online detection of laser induced damages on optical coatings with long distance microscopy

---

Master Thesis

Manuel Mucha

31.08.2015

Supervisor FH: Prof. Dr. Andreas Heinrich

Supervisor DLR: Dr. Helmut Schröder

Manuel Mucha
Matriculation number: 31537

Online detection of laser induced damages on optical coatings with long distance microscopy

Master thesis
Master of Science (Photonics)

University of applied science Aalen

Date: 01.03.2015 - 31.08.2015

Acknowledgment

An dieser Stelle möchte ich mich bei all denjenigen bedanken, die mich während dieser Arbeit unterstützt haben und somit zum Gelingen dieser Arbeit beigetragen haben.

Bedanken möchte ich mich vor allem bei Dr. Helmut Schröder, der mir immer mit Rat und Tat zur Seite stand. Ohne diese uneingeschränkte Hilfe wäre diese Arbeit nicht in diesem Umfang entstanden. Des Weiteren möchte ich mich bei Herrn Wolfgang Riede für die Unterstützung bedanken und für die Chance meine Masterarbeit im DLR anfertigen zu dürfen.

Darüber hinaus gilt mein Dank dem restlichen Team AOS der Technischen Physik des DLR, insbesondere Markus Hippler, Fabian Sproll und Paul Wagner, die mir mit konstruktiver Kritik und Ideen zur Seite standen. Außerdem möchte ich mich bei Gabriele Taube für die Unterstützung an den Mikroskopen und bei Franz Hadinger für die Unterstützung bei Mechanik Fragen bedanken.

Ein weiterer Dank gilt Prof. Dr. Andreas Heinrich für die hochschulseitige Betreuung. Durch die stetige Rückmeldung und die konstruktive Kritik konnten viele Fragestellungen gelöst werden.

Ein sehr großer Dank geht an meine Eltern, sowie an meinen Stiefvater, die mich nicht nur während meines Studiums, sondern auch während dieser Arbeit finanziell und seelisch unterstützt haben.

Zuletzt möchte ich mich bei meiner Freundin Sabrina bedanken. Sie hat immer genug Geduld für michaufbringen können und mich in meinem Tun stets unterstützt.

Abstract

Today's high power pulsed laser applications need optics with coated surfaces to improve the optical characteristics. A major problem of those layers is the lower laser induced damage threshold (LIDT) compared to the pure substrate. For better understanding of damaging process it is quite necessary to investigate how damages occur.

One of these applications are laser systems used in satellites for wind profiling (ADM Aeolus). For best experimental results the testing parameters should be adapted to satellite conditions as good as possible. Therefore all tests are realized in a vacuum chamber under a pressure of 10^{-9} mbar. Furthermore the expected damage size which wants to be observed is in the range of few microns. This is why a long distance microscope is used in this work to investigate the damage formation online.

To show the functionality of system high reflective (coated with ion beam sputtering and electron beam evaporation) and antireflective (coated with ion beam sputtering) coatings are investigated with a repetition rate of 1Hz to acquire images after each pulse. In a next step so called micro pits are investigated in their characteristics and formation. Moreover the dependency of laser repetition rate on LIDT is investigated for rates of 20Hz and 100Hz.

A conclusion and an outlook at which possible improvements and new possibilities are discussed complete this work.

Table of abbreviations

Abbreviation	Description
ADM	Atmospheric Dynamics Mission
AFM	Atomic force microscopy
ALADIN	Atmospheric laser Doppler instrument
Ana	Analyzer
AR	Antireflective
Ar	Argon
Ar^+	Argon ion
B.C.	Before Christ
CCD	Charge coupled device
CF	Conflat
Cond	Condensing lens
cw	Continuous wave
DIC	Differential interference contrast
DLR	German Aerospace Center
DN40/DN63	Description for vacuum flanges
EBE	Electron beam evaporation
ESA	European space agency
FWHM	Full width half maximum
HR	High reflective
HT	High transparent
HV	High vacuum
IBS	Ion beam sputtering
IR	Infrared
ISO	International organization for standardization
IV	Ideal vacuum
KD*P	Potassium dideuterium phosphate
LDM	Long distance microscope
LED	Light emitting diode
LIDT	Laser induced damage threshold
MCP	Multi-channel plate

Nd:YAG	Neodymium-doped yttrium aluminum garnet
Obj	Objective
OPD	Optical path difference
Pol	Polarizer
PSI	Phase shifting interferometer
ROI	Region of interest
SHG	Second harmonic generation
SI	Systeme international d'unites
SP	Scroll pump
Spec	Specimen
THG	Third harmonic generation
Tif	Tagged image format
TMP	Turbo molecular pump
UHV	Ultra high vacuum
UV	Ultra violet
W	Wollaston prism
WLIM	White light interferometer microscopy
XHV	Extreme high vacuum

Table of prefix, units and symbols

Prefix	Description
k	Kilo, 10^3
h	Hecto, 10^2
c	Centi, 10^{-2}
m	Milli, 10^{-3}
µ	Micro, 10^{-6}
n	Nano, 10^{-9}

Unit	Description
bar	Bar
eV	Electronvolt
Hz	Hertz
J	Joule
K	Kelvin
m	Meter
Pa	Pascal
rad	Radiant
s	Second
V	Volt
W	Watt
%	Percent

Symbols	Description
A	Area
d	Thickness
dz	Coherent length
E_p	Pulse energy
F	Force
H	Fluence
L	Length
n	Refractive index
p	Pressure
R	Reflectivity
r	Reflectivity of single layer
x, y	Coordinates
α, β	Angles
δ	Phase shift
Δ	Delta
λ	Wavelength
π	Pi (= 3.14)
τ	Pulse duration
ω	Beam diameter

Table of contents

1 Introduction

In the era of photon the light became the most important tool of our daily routine for our own use or for manufacturing high precise electronics as well as in medical applications. It is difficult to find a section in our life where we do not use light somehow.

A lot of applications use pulsed high power lasers and each of these systems need optics to guide or to shape the beam as required. Nearly all optics are coated for improving the optical characteristics. However some disadvantages have to be accepted by improving optics with coatings. One of these drawbacks is the drop of laser induced damage threshold (LIDT). This means that less energy is needed to create damage at coated surfaces compared to pure substrates. [1]

Finally the laser induced damage threshold limits the maximum energy level of a laser system. Therefore it is quite desirable to improve the optical coatings and furthermore it is extremely important to understand the complete process of damage formation to get knowledge at which parameters damages start and how they grow until a certain number of pulses is reached.

One of the applications, where such a combination of pulsed high power laser and coated optics can be found, is a laser-based satellite, for instance the Aeolus satellite which should be launched in 2016. This ESA (European Space Agency) mission got its name from the Greek Lord of wind Aeolus because main task of this satellite is the profiling of winds from low earth orbit (~408 km height). Therefore a pulsed laser system with a wavelength of 355 nm is used which is called ALADIN (Atmospheric Laser Doppler Instrument). For guiding and shaping the laser beam, the system contains coated optics which are tested in the Institute of Technical Physics at German Aerospace Center. [2] [3] [4]

Figure 1: The Aeolus satellite with ALADIN laser instrument to profile the world's winds. Also a sketch of Greek Lord of winds Aeolus is seen on the left side of image.[1]

1.1 State of technology

The characteristical thresholds for optics and coatings are well known and investigated by many scientists and experiments. Also for investigating characteristical features of damages, many tests are done so far.

Current situation is that damage thresholds in optical coatings are mainly measured by scattered light. Therefore a sensor detects the change of scattered light and just over a trend damages can be detected. The main problem is that damages smaller than 10 µm are leading to diffraction effects. This means that the solid angle of scattered light is very large and therefore less signal hits the detector. Finally the detector realizes a damage not before it reaches a certain size.

Another point is that the measurement of scattered light do not allows a statement about the dynamic of damage formation.

[1] http://cdn.physorg.com/newman/gfx/news/hires/2013/1-90millionlas.jpg

1.2 Goal of the thesis

The goal of this thesis can be separated in two parts. On the one hand it is quite important to understand the process of damage formation much better. On the other hand it is just as important to evaluate a new approach for online detection of damages at an early state of damaging process. Therefore the method needs to have a higher spatial and temporal resolution such as the actual method.

The first part of this work is therefore the set-up of a test bench which achieves these requirements. The test bench with all its components is discussed in chapter 3. In a next step the insitu monitoring of dynamic of damage formation should be realized. Therefore several coatings are investigated and the results are discussed in chapter 4. Chapter 5 deals with the optimization of the setup.

Main tool for online detection is a so called long distance microscope which is basically a Maksutov-Cassegrain telescope. Main advantage is a very large working distance compared to classical microscopy. Nevertheless with this type of microscopy a good resolution can be reached in spite of the large distance between objective and object.

2 Basics

2.1 Laser induced damage threshold (LIDT)

At each optical component damage can be created by a high power laser when the target is irradiated over a specific limit. This limit is called laser induced damage threshold and is abbreviated with LIDT [1]. In case of pulsed laser the unit for LIDT is J/cm² (see next chapter). In the frame of this work fluence means always the peak fluence for pulsed lasers.

The damage can occur at the surface or in the bulk. The International Standard ISO 21254 defines surface damages as the change of characteristics of the surface of a specimen. When bulk damage occurs the optical characteristics inside the optical component are changed. Therefore different inspection techniques for surface damages and bulk damages are required [5].

In case of this thesis damages are expected on the surface of target and the LIDT value depends on the wavelength of laser beam, pulse duration, pulse rate, spot size and angle of incidence. For comparison of results these parameters have to be defined for each experiment [1].

The reasons for damages in optical components are widely spread. The most important cases are thermal effects due to absorption and dielectric breakdown. Essentially it depends on pulse duration which effect happens. At long pulses in a region from continuous wave to ~10^{-8}s thermal absorption induces damages. Shorter pulses from 10^{-8} s – 10^{-10}s create dielectric breakdowns because the photons have such a high energy density to split the chemical bonding of target material directly. When the pulse duration is even shorter avalanche ionization and multiphoton absorption can occur. In the frame of this thesis, a laser with pulse duration of 3.5 ns was used and therefore it is not essential to consider effects on shorter pulse durations. Other effects which can generate damages are defects in the material itself. Impurities, scratches or other defects in optical materials or coatings could increase the absorption which reduces the LIDT. Other effects are self-focusing and nonlinear effects. For further information about these effects see [6].

2.2 Fluence

The LIDT value is issued with fluence (H) for pulsed lasers because this is the best way to standardize the threshold values for better comparison. But it is necessary to note the experimental conditions for each LIDT result.

The peak fluence is the equivalent to irradiation of radiometric dimensions and is given with the peak energy (E_p) of laser pulse which drops on an effective focal spot area [7].

In case of Gaussian beam profile the fluence is defined by the ratio of twice the pulse energy and the area which depends on beam diameter [8].

Equation 1: Peak fluence for Gaussian beam

$$H = \frac{2 * E_p}{\pi * \omega^2}$$

For a non-perfect Gaussian profile the beam radius is split into x and y-value due to the elliptical profile (see Equation 2) [8].

Equation 2: Peak fluence for Gaussian beam with elliptical profile

$$H = \frac{2 * E_p}{\pi * x * y}$$

In a last step we have to consider that the sample is irradiated under an angle of 45°. Hence the length of beam profile increases only in x-direction by a factor of cos (45°) (see Equation 3) [9].

Equation 3: Peak fluence for Gaussian beam with elliptical profile under an incidence angle of 45°

$$H = \frac{2 * E_p}{\pi * \frac{x}{\cos(45°)} * y}$$

2.3 Vacuum physics

Since Demokrit, a Greek philosopher (460 to 375 B.C.) who was the first who talked about vacuum, a lot of scientists did many different experiments to understand the nature of vacuum. In last three centuries engineers used this knowledge to design pumps to generate vacuum and to measure it [10]. This section gives an introduction about the essential knowledge of vacuum physics.

In a first step it is crucial to define pressure and vacuum. Pressure (p) is defined as the force (F) which acts on a defined area (A) (see Equation 4) [10].

Equation 4: Relationship between pressure (p), force (F) and area (A)

$$p = \frac{F}{A}$$

Corresponding to the SI system Pascal (Pa) and bar are used as units for pressure. The relationship between these two units is given as [10]

$$1\ mbar = 100\ Pa = 1hPa$$

In case of vacuum chambers the force is caused by gas which fills a certain volume homogenously. Therefore pressure is decreasing by increasing the volume or by decreasing the amount of gas. Per ISO 3529/1 [11] vacuum is defined as the condition of a gas, when the pressure or the number density of molecules is lower than at atmospheric pressure. For generating vacuum in a chamber the number density of molecules can be reduced until a minimum which is defined by the system parameters. This process is called evacuation [12].

Moreover there exists some important definitions of different pressures. The standard atmospheric pressure is defined in ISO 3529/1 [11] as the surrounding air pressure at sea level and has a value of 1013.25 mbar. The lowest pressure which can be reached in a certain vacuum chamber is called final pressure but it is an ideal value which only can be reached under perfect conditions. The final pressure should not be mixed with the working pressure which can be reached under real conditions [13].

Table 1 gives an overview about the vacuum ranges. Displayed are pressure, number density of molecules, mean free path and typical vacuum application. The pressure depends on temperature and number density of molecules. By decreasing pressure the possibility that molecules strike each other is also decreased. The mean free path is a value for the distance of a molecule between two collisions [12] [13].

A more detailed overview is given in the appendix (see Figure 66). This image also shows the vacuum ranges of earth atmosphere.

Table 1: Overview of vacuum [12] [14]

Pressure range	**Pressure in hPa (mbar)**	**Molecules in 1/cm³**	**Mean free path**	**Typical vacuum applications**
Standard atmospheric pressure	1013.25	2.7×10^{19}	68 nm	
Low vacuum	300…1	10^{19}…10^{16}	0.1…100 µm	Vacuum packaging, bulb
Medium vacuum	1…10^{-3}	10^{16}…10^{13}	0.1…100 mm	Gas discharge lamp
High vacuum (HV)	10^{-3}…10^{-7}	10^{13}…10^{9}	100 mm …1 km	Electronic tubes, Cern ion trap
Ultra high vacuum (UHV)	10^{-7}…10^{-12}	10^{9}…10^{4}	1…10^{5} km	Low earth space, semiconductor manufacturing
Extreme high vacuum (XHV)	< 10^{-12}	< 10^{4}	>10^{5} km	Space
Ideal vacuum (IV)	0	0	∞	Cannot be achieved and measured technically

2.4 Basics of evaluation methods

2.4.1 Maksutov-Cassegrain telescope

A Maksutov-Cassegrain telescope is basically a Cassegrain setup (1672) which is optimized by Maksutov in 1942.

The Cassegrain telescope has a parabolic mirror (concave) with a short focal length. A hole is drilled through the center of this primary mirror. Furthermore a hyperbolic mirror is located vis-à-vis to the primary mirror and focuses the image through the hole of primary mirror into the focal plane. In spite of the short tube length with this special setup a high focal length can be reached. [15]

Due to the fact that the second mirror extends the focal length of primary mirror, the second mirror requires a relatively large diameter in a range of 35-40 % to primary mirror. The central rays of optical system are shadowed and are not imaged.

But at the edges of the secondary mirror the waves are diffracted and therefore the contrast is reduced. Another disadvantage is aberration of primary mirror like spherical aberration, coma and astigmatism from off-axis rays. [16]

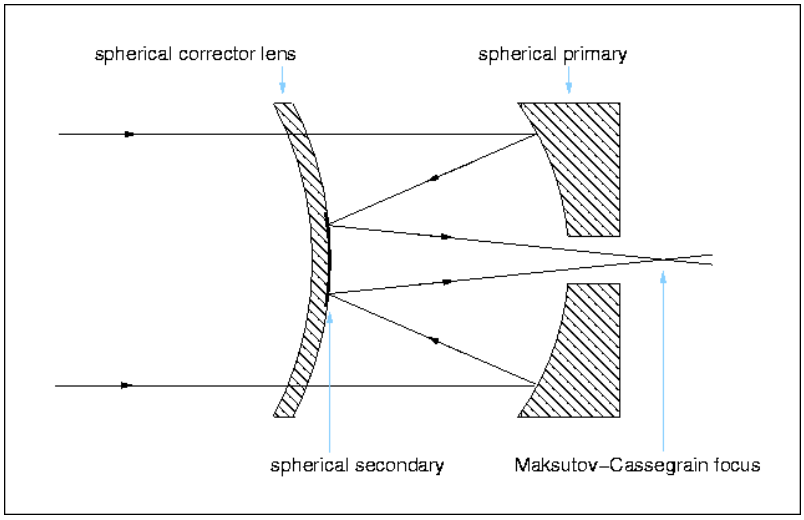

Figure 2: Setup of a Maksutov-Cassegrain telescope with spherical corrector lens, secondary mirror and primary mirror (from left to right). [2]

[2] http://www.vikdhillon.staff.shef.ac.uk/teaching/phy217/telescopes/maksutov.gif

At this point Maksutov started his development and put a meniscus lens (concave-convex) in front of primary mirror. At the lens's backside the secondary mirror is located which is much smaller compared to the secondary mirror of Cassegrain telescope. Therefore the contrast of the upgraded system is much better. The main advantage of this setup is the independency of curvature from primary mirror to the shape of meniscus lens. This means that meniscus lens corrects the spherical aberration and coma. [17]

2.4.2 Differential interference contrast microscopy

The differential interference contrast (DIC) microscopy was developed by Nomarski and it is based on polarization microscopy. With this technology the optical path length for different densities in the material is set into a contrast image. [18]

In a first step it is important to create linear polarized light with a polarizer (Pol). In a next step a birefringent prism (W_1), so called Wollaston prism, splits the linear polarized beam into two beams with same amplitude which are perpendicular polarized to each other. These two beams are parallel but have a mismatch in between. This mismatch has to be less than the resolution limit of microscope's objective. With a condensing lens (Cond) these two beams are focused in the sample plane (Spec). Due to thickness and density of material the beams are changed in their phase and we get a phase shift between these two beams. After microscope's objective (Obj) a second Wollaston prism (W_2) brings the two beams together and an analyzer (Ana) makes the beams interfering. [19]

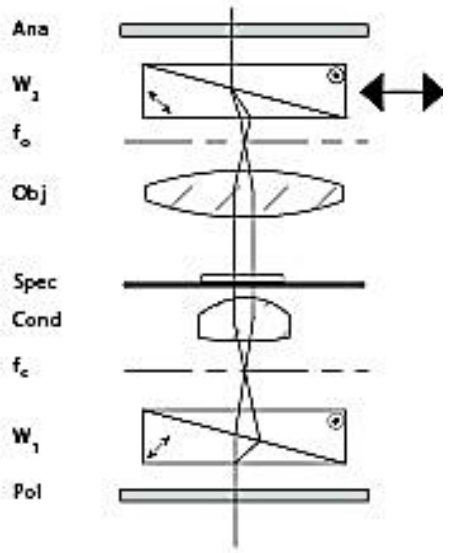

Figure 3: Schematic setup of differential interference contrast microscopy.[3]

At edges of damages or scratches inside the sample there is a phase shift between both beams. Therefore also the amplitude is getting changed and the edges get a very high contrast which generates a 3-dimensional effect. [19]

2.4.3 White light interferometry

For this type of interferometer the basic Michelson setup is used (see Figure 4). This means the illumination beam is split into a reference arm and a measurement arm by a beam splitter. The beam in reference arm is reflected by a plane mirror and beam in measurement arm is illuminating the sample. Both beams are recombined by the beam splitter and interfere at CCD detector. The interferometer scans the sample in z-direction and generates a 3-dimensional profile of the sample. With this technology many different kinds of surfaces can be profiled with an accuracy of few nanometers. [20]

[3] http://microscopy.berkeley.edu/Resources/instruction/images/DIC4.jpg

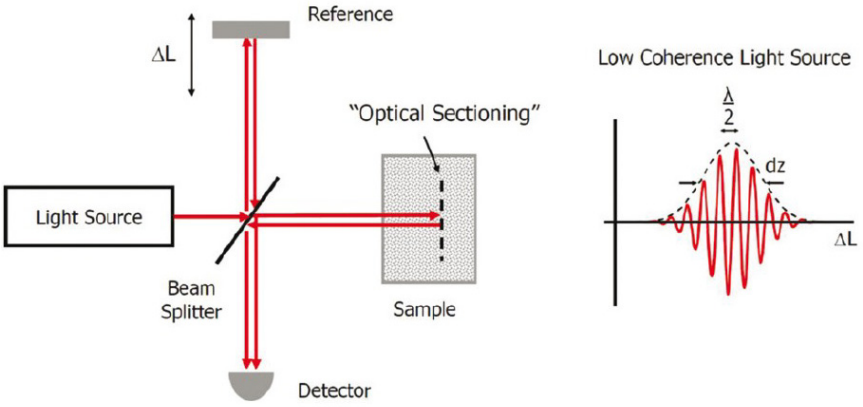

Figure 4: Schematic of white light interferometer based on Michelson interferometer setup. [4]

When optical path difference (OPD between reference arm and measuring arm) in an interferometer is smaller than the coherence length, interferences occur. For a high dynamic range, the use of a light source with short coherence length is necessary. This is why white light instead of a monochromatic laser light is used in this kind of interferometer (see Figure 5). [21]

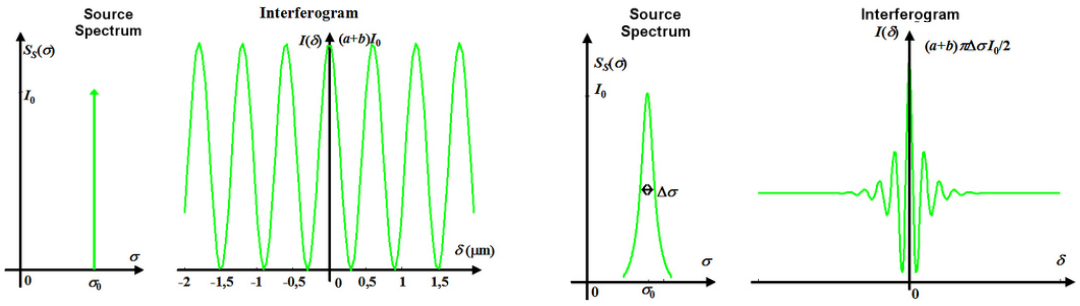

Figure 5: Interferogram of monochromatic source with long coherence length (left) and interferogram of white light source with short coherence length (right). [5] [6]

In addition for higher resolution the phase shift can be evaluated. This technique is called PSI (phase shifting interferometry). In contrast to the upper technique monochromatic light is used and information about the surface height is obtained from the phase shift. The

[4] http://jpathinformatics.org/articles/2012/3/1/images/JPatholInform_2012_3_1_22_96751_u4.jpg
[5] http://www.optique-ingenieur.org/en/courses/OPI_ang_M02_C04/res/fig_12_C.jpg
[6] http://www.optique-ingenieur.org/en/courses/OPI_ang_M02_C04/res/fig_09_C.jpg

main advantage of this type of interferometry is the higher accuracy of few sub-nanometers. [22]

2.4.4 Atomic force microscopy (AFM)

The atomic force microscope is compared to the other discussed methods a mechanic technique. With such a microscope, topographies of surfaces in nanometer range can be generated by measuring the force between a probe and the surface. A microscopic tip is fixed at the end of a cantilever which scans the surface line by line. The forces of the surface structure are deflecting the tip and also the cantilever. On the back of the cantilever a laser beam is focused which is reflected to a sensor. By this method the deflection of cantilever can be measured and transformed into a 3-dimensional profile of investigated surface. The resolution is determined by the tip and is in the range of 0.4 nm in z-direction and 1.7 nm in x-y-direction (values for used AFM). Due to this high resolution a very low scanning speed is achieved which makes the whole system quite slowly. [23] [24]

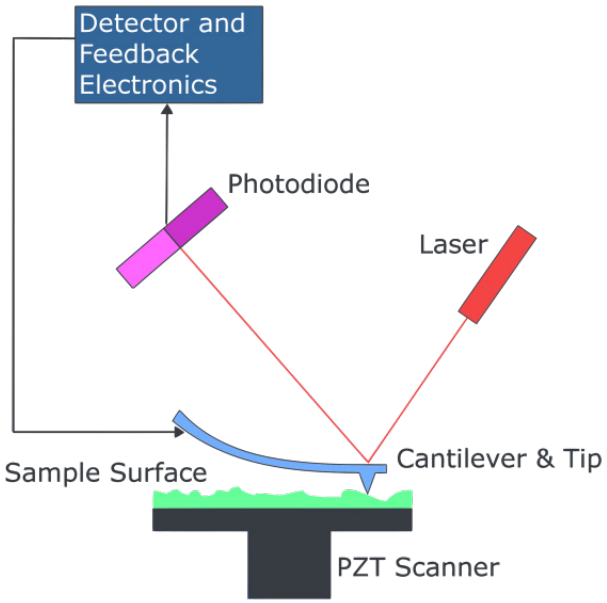

Figure 6: Principle of atomic force microscopy with PZT scanner, cantilever with tip, laser, photodiode and sample.[7]

[7] https://upload.wikimedia.org/wikipedia/commons/thumb/7/7c/Atomic_force_microscope_block_diagram.svg/2000px-Atomic_force_microscope_block_diagram.svg.png

There are several scanning modes which are used in the AFM technique. In the contact mode the tip is always in direct mechanical contact with the sample. The disadvantage of this method can be the deformation or destruction of surface or tip. Also the resolution is limited to dimensions of tip. The method which compensates those disadvantages is called non-contact mode. The cantilever is stimulated to oscillate with its resonant frequency near sample surface. When a force between tip and surface appears, due to change of surface structure, a phase shift can be measured.

Other disadvantages of AFM are vibrations beyond the system, thermal drifts as well as electrostatic charging. But nevertheless the extreme high resolution makes this kind of microscopy very useful for surface investigation. [23] [24]

2.5 Optical coating

Optical materials, i.e. fused silica, are finally developed to a maximum of quality. As Figure 7 shows the transmission of fused silica in the UV and IR range is quite good but cannot reach 100% due to physical limits. These limits depend on the transition of refractive index at the interface between air and substrate. This is why nearly each high performance optic is coated with a thin film for its specific application. There are high-reflective coatings for mirrors from UV to IR range available. Another coating type is the anti-reflective one which can be found on glasses or high power optics where the reflectivity of a surface should be reduced to a minimum. For the UV range is fused silica a good choice due to already high transmittance in this spectral range. HR and AR coatings are introduced in this chapter as well as the manufacturing technologies Ion Beam Sputtering and Electron Beam Evaporation.

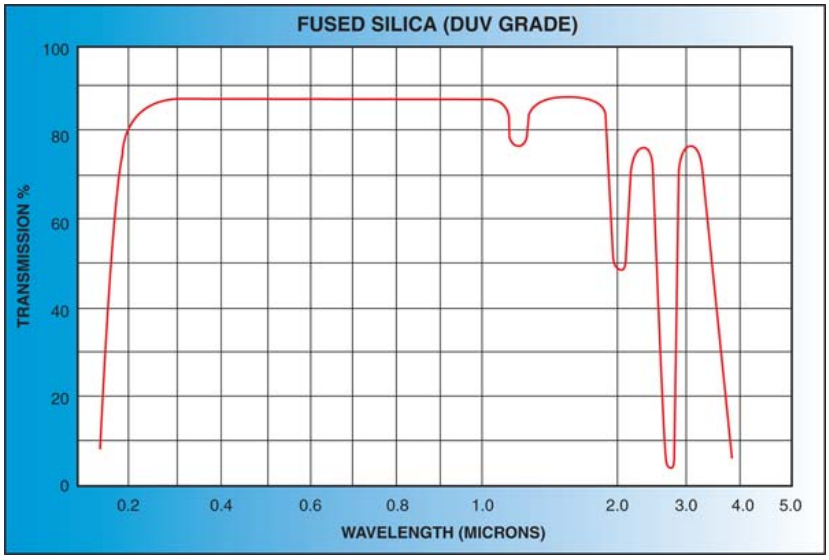

Figure 7: Transmission curve of fused silica as a function of wavelength.[8]

2.5.1 Theory of thin film coatings

This chapter introduces the principle physics of thin film coatings for high reflective and antireflective coatings. Optical interference forms the basis of those optical components. At first a substrate with a single layer is considered. The thickness of those layers, regardless of which type of coating, is given with the phase shift which is a function of the wavelength (λ) and the optical thickness (n_1 x d) (see Equation 5). [25]

Equation 5: Phase shift after passing the thin film

$$\delta = \frac{2\pi}{\lambda} n_1 d$$

For an optical thickness of λ/4 the phase shift is π or an odd multiple of π due to the fact that the light is traveling twice the optical thickness. For this special case the phase shift of π causes destructive interference. This effects a maximum change in gain or extinction of reflection. [26]

The reflectivity at a single surface is given with the Fresnel reflectance law and is a function of the refractive index of both adjacent materials. In Equation 6 it is given for an angle of incidence of 0°.

[8] http://www.lesker.com/newweb/flanges/jpg/chart/Chart-HD-FusedSilicaDUVGrade_01.jpg

Equation 6: Fresnel reflectance law for an angle of incidence of 0°.

$$R = (\frac{n_0 - n_1}{n_0 + n_1})^2$$

The allocation of refractive indices can be taken out of Figure 8 which shows the principle reflectance of light at surfaces of thin films.

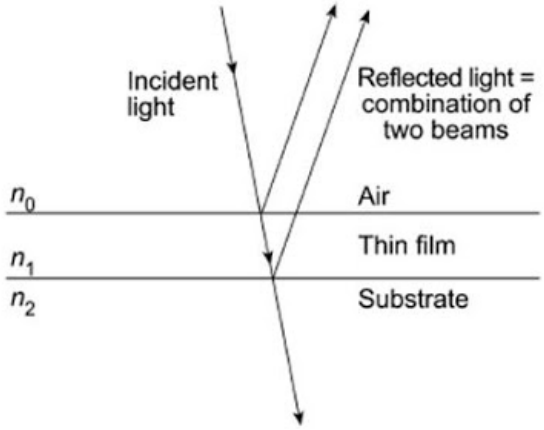

Figure 8: Principle reflectance of light at surface of thin film.[9]

By consideration of a single layer system with two surfaces the Equation 7 is given. If $n_1 > n_2$ the reflectivity is increased and a high reflective layer is created. In case of $n_1 < n_2$ the reflectivity is decreasing and antireflective coating is produced. In the special case of $n_1 = \sqrt{n_0 * n_2}$ the reflectivity is reduced down to zero but only for a certain wavelength. For nearby wavelengths the reflectivity is increasing again. [27]

Equation 7: Fresnel formula for reflectivity of single layer system with an optical thickness of λ/4 for an angle of incidence of 0°.

$$R_{\lambda/4} = (\frac{n_0 * n_2 - n_1^2}{n_0 * n_2 + n_1^2})^2$$

9 http://4.bp.blogspot.com/_CIK7hYCrWhk/TD4LQZaT2QI/AAAAAAAAAtg/DRH7cIHaZ_g/s640/1.JPG

To improve the characteristic of coatings more than one layer is deposited on the substrate. Those coatings are called multilayer coatings and are available for HR coatings as well as AR coatings. The most applications of such coatings are the minimization or maximization of reflection for more than a single wavelength. The final reflectivity is a function of the individual reflectivity and the phase shift. An example for two layers is given with Equation 8. [27]

Equation 8: Fresnel formula for a multilayer coating with two layers.

$$R_{multi} = \frac{r_1^2 + r_2^2 + 2r_1 r_2 \cos 2\delta}{1 + r_1^2 r_2^2 + 2r_1 r_2 \cos 2\delta}$$

This formula can be expanded for large number of layers but also complexity is increasing enormously.

2.5.2 Fabrication of optical coatings

In this work for investigation of damage formation high reflective and antireflective coatings were used. The HR samples are coated with ion beam sputtering (IBS) or with electron beam evaporation (EBE). The AR coatings are coated with IBS technology.

2.5.2.1 Ion beam sputtering

Ion beam sputtering is the most common technology to coat optics for high power application. A high energy ion gun emits ions by approximately 1.5 kV onto a target material. The ions sputter single atoms out of the target material which consists of desired coating compound. Those ablated atoms are travelling to a rotating substrate and condense on it. [28] The whole process is realized under high vacuum which reduces the collision from ablated atoms with oxygen or other molecules in the chamber. [29] Kinetic energy of up to 10 eV of those atoms and the low collision rate produces coatings with an excellent microstructure and high packing density. This can be explained by the fact that the atoms with such a high energy are not bound on a specific location at the depositing layer. The high flexibility let them take the best possible position in the layer. This is why ion beam sputtering creates homogenous and dense coatings. [30]

The only disadvantage of this technology is the low deposition rate compared to electron beam evaporation. [31]

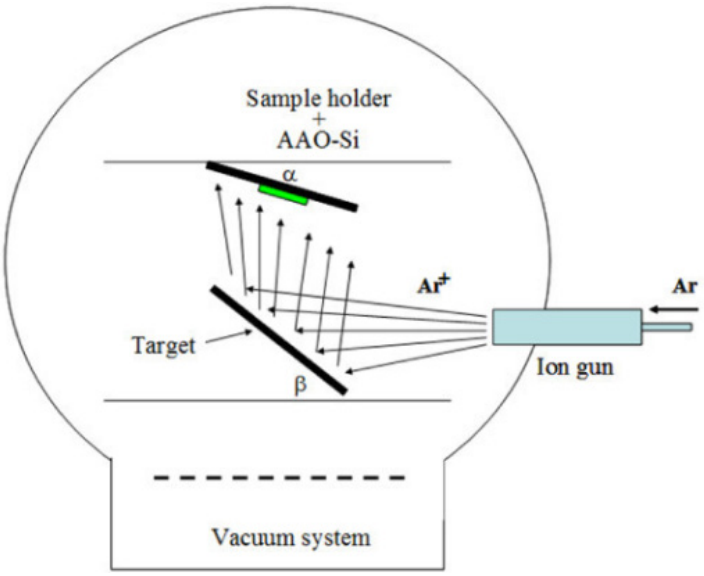

Figure 9: Principle of ion beam sputtering in a vacuum chamber with argon ion gun shooting ions on target material. Ablated atoms from target condense on substrate.[10]

2.5.2.2 Electron beam evaporation

At Electron Beam Evaporation electrons instead of ions compared to IBS are emitted and bombard the target material. The target material is heated until the atoms are vaporized. Just as well at IBS the atoms travel through a vacuum and condense on the substrate. [29] But those atoms have a much lower kinetic energy of 0.1 eV to 0.2 eV which creates a porous layer with a low packing density. [32] Advantage of EBE is the high evaporation rate and therefore the fast process velocity. [28]

[10] http://openi.nlm.nih.gov/imgs/512/0/3212010/3212010_1556-276X-6-495-1.png

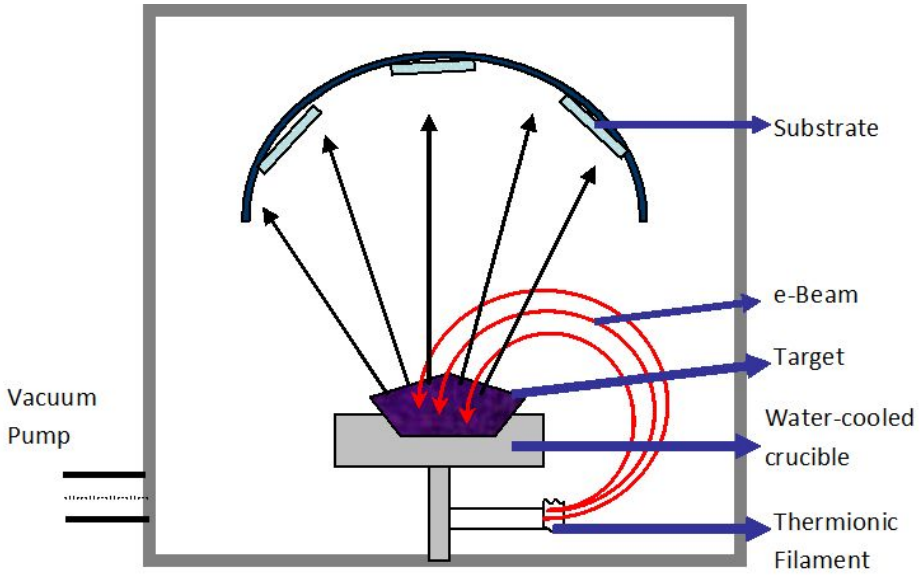

Figure 10: Principle of electron beam evaporation in a vacuum chamber with thermionic filament which emits its electrons on target material. Ablated atoms from target condense on substrate.[11]

[11] http://www.intechopen.com/source/html/39997/media/image5_w.jpg

3 Test bench

In the frame of this work a test bench for LIDT experiments has to set up. In general the components are split in the sections light source, vacuum chamber, optical setup and detection. The following chapter gives an overview about the used devices.

3.1 General setup

This section deals with the general setup with all its components which is shown in Figure 11.

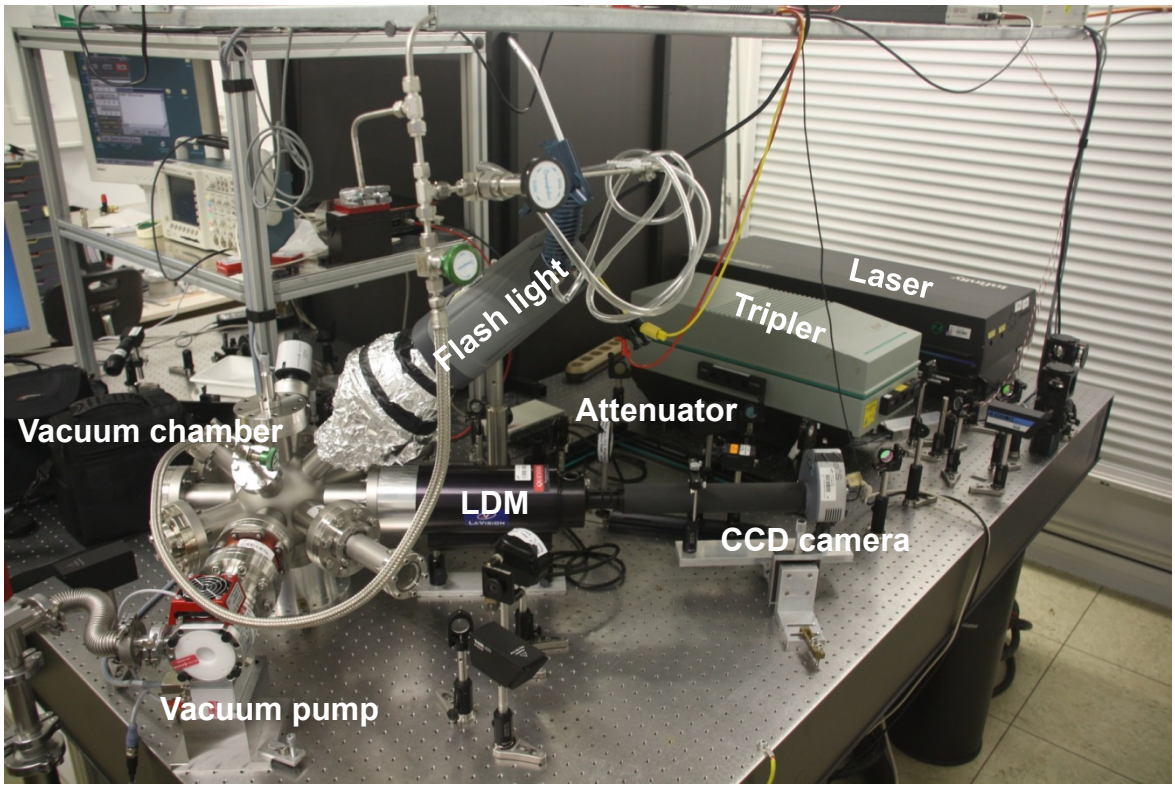

Figure 11: Experimental setup with the components laser, tripler, optical beam line with attenuator and focusing lens, LDM with flash light, vacuum chamber, vacuum pump and measurement devices.

The IR beam (1064 nm) which is created in the Nd:YAG laser is guided through a tripler which made 355 nm out of IR beam. This beam is guided through an attenuator which is setting the final fluence. An additional lens is focusing the UV laser beam in sample plane and creates damages at sample specific fluences. The sample is located in a vacuum chamber which is evacuated by a pumping system. The main online investigation (insitu) is realized by a long distance microscope. Finally there are additional measurement devices which measure the pressure in the vacuum chamber or characterize the fluence which hits the sample.

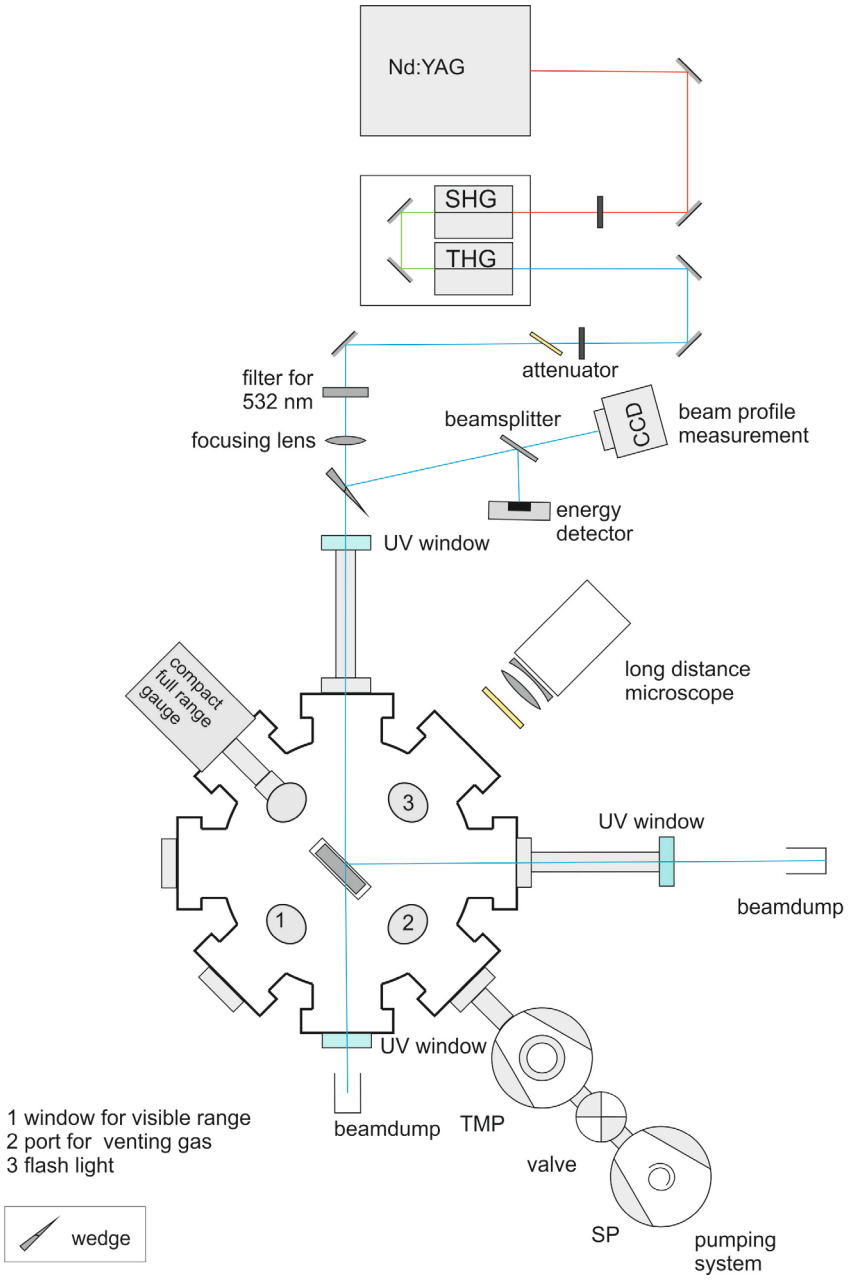

Figure 12: Sketch of general setup

3.2 Light source

3.2.1 Laser

As light source the Infinity™ from Coherent is used. The gain medium of the solid state laser consists of neodymium doped yttrium-aluminum-garnet crystal followed by an amplifier stage. As pump source a flash lamp is used and the pulses are achieved by Q-switch technology. The output energy can be varied by changing the voltage of flash lamp [33]. The characteristics pulse duration, divergence, pulse to pulse stability, depolarization and noise of Infinity laser were determined prior to the damage tests and are listed in Table 2.

Table 2: Laser specifications of Infinity laser from Coherent.

Parameter	Value
Wavelength [nm]	1064
Pulse energy [mJ] @ 1064 nm, 100 Hz	1…400
Pulse energy [mJ] @ 1064 nm, 20 Hz	1…500
Pulse energy [mJ] @ 1064 nm, 1 Hz	1…600
Pulse duration (FWHM) [ns] @ 1064 nm, 100 Hz, 30 mJ	3.4 ± 0.2
Divergence [mrad]	0.9
Pulse-to-Pulse variation [%] (over 20 pulses)	< 43.6 @40 mJ < 21.56 @70 mJ < 9.48 @180mJ
Repetition rate [Hz]	0.1 … 100
Depolarization [mJ]	0.34 @30 mJ 0.56 @70 mJ 0.74 @100 mJ 1.80 @200 mJ
Noise [%]	15.2 @30 mJ 7.5 @70 mJ 5.2 @100 mJ 2.9 @200 mJ

The parameters pulse energy and repetition rate are adjustable and can be changed by laser software. During first experiments pulse energy of 70 mJ is adjusted. In last

experiments the flash lamp voltage is set to 500 V which corresponds to output energy of nearly 220 mJ. This has the advantage that the laser runs with a higher pulse to pulse stability. To avoid thermal effects, the laser needs a warm up time of several minutes to get stable.

3.2.2 Generation of UV light

The generation of UV light out of IR radiation from the Nd:YAG laser is realized by frequency tripling using BAP Tripler from Continuum. Figure 13 shows the schematic of the optical layout for BAP tripler. By a wave plate the polarization of incoming IR beam (1064 nm) can be adjusted. A HR mirror (highly reflective at 1064 nm) guides the beam through a KD*P (Potassium Dideuterium Phosphate) crystal. In this nonlinear crystal 532 nm is generated by frequency doubling. But this conversion is not complete and therefore IR light is remaining. In a second KD*P crystal the 532 nm and 1064 nm light is converted to 355 nm by sum-frequency generation. Behind the crystals are two dichroic mirrors which separate the UV light from non-converted 532 nm and 1064 nm light (HR 355 nm, HT 1064 nm, HT 532 nm).

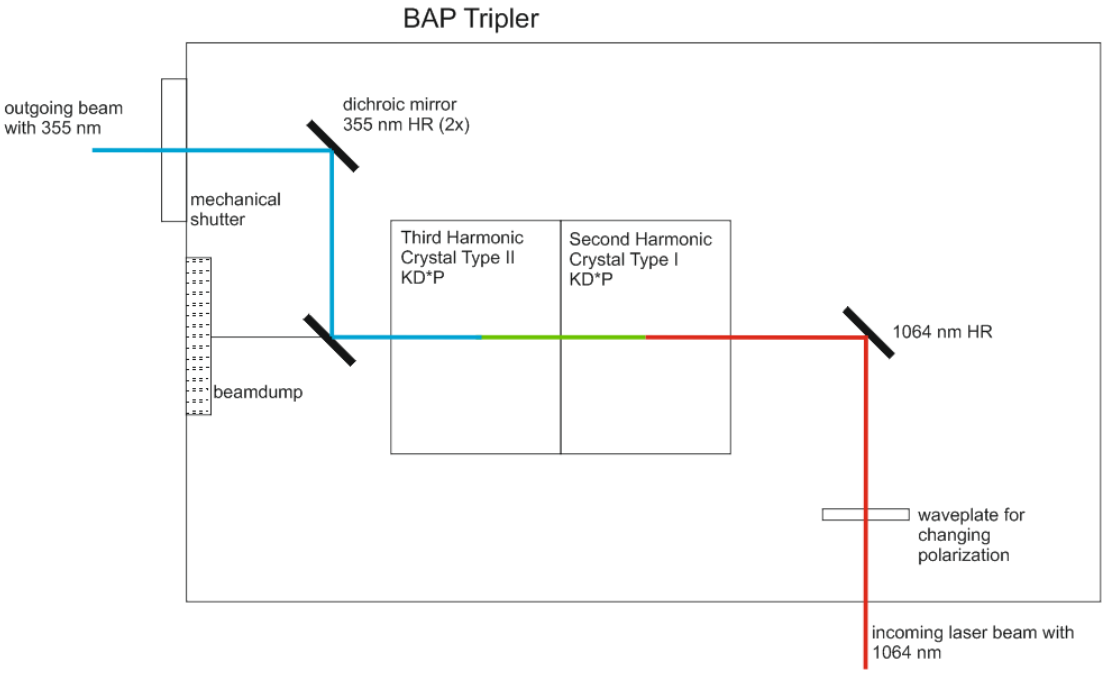

Figure 13: Schematic of optical layout for BAP Tripler [34]

3.2.3 Characterization of laser parameters

Several testing parameters are sufficient to characterize the LIDT of optical coatings. The most important parameters are wavelength, pulse duration, repetition rate, spot size and angle of incidence (see chapter 2.1). The wavelength is fixed to 355 nm. Also the angle of incidence is fixed to 45° during the complete test duration. The only manually changed parameter is the laser repetition rate. For first tests it is set to 1 Hz but for further investigation also 20 Hz and 100 Hz are used. Some first tests show a dependency of fluence on repetition rate.

The influence of pulse duration on the LIDT value is given by the following Equation 9. [1]

Equation 9: Laser induced damage threshold as a function of pulse duration.

$$LIDT_2 = LIDT_1 * \left(\frac{\tau_2}{\tau_1}\right)^x \qquad ; for\ x = 0.3 \dots 0.8$$

The formula shows that a change in pulse duration effects a change in LIDT. On the other hand the effective area influences the LIDT directly. Therefore the parameters pulse duration and spot size have to be precisely characterized.

The effect of decreasing pulse energy is a well-known consequence of increasing repetition rate which is confirmed by the lasers manual [33]. The pulse duration is measured with the help of photodiode and oscilloscope.

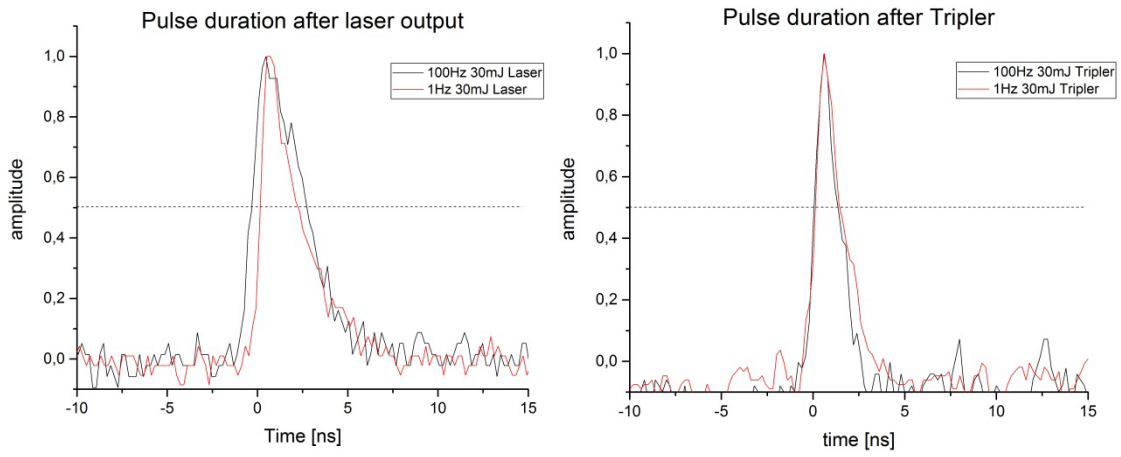

Figure 14: Measured pulse duration for 100Hz and 1Hz repetition rate at 30 mJ laser output energy, directly after laser output (left hand side) and directly after tripler (right hand side).

Figure 14 shows the dependency of pulse duration on repetition rate. For comparison the full width half maximum (FWHM) values are used. It can be seen that pulse duration decreases by decreasing repetition rate. But this is only true for the IR beam directly measured after laser output. When UV beams from the Tripler output are investigated, the pulse duration for both frequencies are narrowed to same duration.

The next parameter which is checked is the spatial profile of laser beam. The measurement is realized after tripler output briefly before the beam enters the vacuum chamber. The results are displayed in Figure 15 for 100Hz repetition rate (left) and 20Hz repetition rate (right).

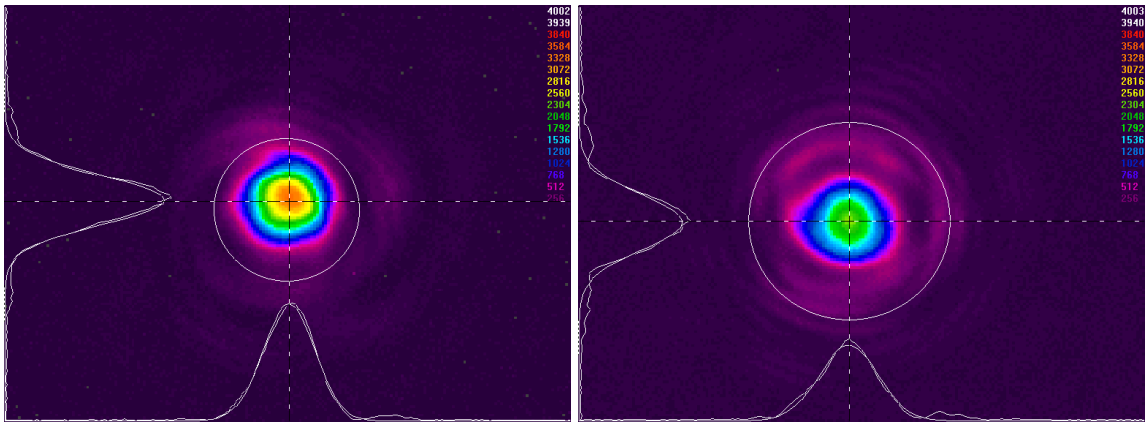

Figure 15: Spatial profile of laser beam after UV conversion; for 100Hz repetition rate (left hand side) and 20Hz repetition rate (right hand side).

The beam analyzer program calculates a Gaussian fit function directly and gives as result the values for diameter in x and y-direction.

Table 3: Measured values for spatial profile of laser beam running at 100Hz and 20Hz repetition rate. Calculated values for area and fluence out of measured values are displayed as well as calculated fluence for energy of 550 µJ.

Repetition rate [Hz]	Diameter in x-direction [µm]	Diameter in y-direction [µm]	Area [cm²]	Fluence [J/cm²]
20	185.9	179.7	$5.0*10^{-4}$	2.2
100	169.1	150.8	$3.8*10^{-4}$	2.9

In Table 3 the measured values for spatial profile of laser beam for 100Hz and 20Hz repetition rate are displayed. Also the corresponding values for the effective area and the fluence at 550 µJ energy are shown. It can be seen that the spatial profile at 20Hz is much larger than the profile at 100Hz. To get comparable fluence values the pulse energy has to be adjusted accordingly.

3.3 Vacuum system

This chapter answers the question why a vacuum environment for testing optical coatings for space application is necessary and presents the used chamber with its components.

The reason for the use of vacuum chamber is the adaption of testing parameters on further application conditions. Due to the space based application a vacuum chamber is needed, which generates ultra-high vacuum (UHV) in a range of 10^{-9} mbar which corresponds to a vacuum in 500 km height in earth orbit.

In [35] the air-vacuum effect for dielectric coatings is discussed. The experiments of this paper show a dependency of LIDT on surrounding environment. According to this paper, the LIDT value for EBE coatings is lower for tests in vacuum compared to measurements at ambient atmosphere. For ion beam sputtered coatings such an effect was not observed. This can be explained by the porous structure of electron beam coatings. Water molecules are adsorbed into the free space which is dehydrated under vacuum. This in turn increases the tensile stress in the layer of coating and decreases the LIDT. At IBS coatings, the density of layer material is higher and water molecules cannot be adsorbed.

3.3.1 Vacuum chamber

The vacuum chamber is specially designed for LIDT experiments (see Figure 16). The main body of the chamber is a stainless steel sphere with diameter of 160 mm. The sphere has several standardized CF-flanges of DN63 and DN40. DN63 are the bigger ports. One of them is used for connecting the pumping system to the chamber. The entrance, exit and observation windows for long distance microscopy are also positioned at such flanges. The other DN63 ports are in reserve for further experiments with contamination materials or for advanced measurements. The DN63 flange on top of the chamber is used as input port for the samples. Therefore a special sample holder is

created which is combined with an adjusting screw. The four DN40 flanges are used for the vacuum measurement system, for a venting valve and for two observation windows. All parts are sealed by copper rings.

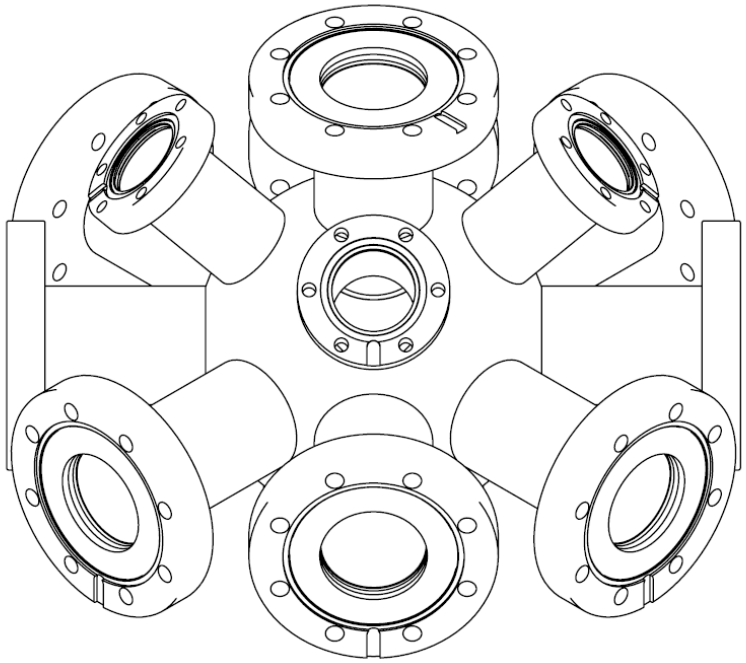

Figure 16: Vacuum chamber

3.3.2 Pumping system

Vacuum pumps are characterized by the final pressure which can be generated by them. A turbo molecular pump for example can produce vacuum up to 10^{-10} mbar. For generating ultra-high vacuum in a test chamber generally a pumping system consisting of fore and main pumps is needed. An oil free scroll pump from Leybold is used as fore pump. This pump evacuates the chamber to a final pressure of 10^{-2} mbar [36]. Between fore pump and vacuum chamber a turbo molecular pump (HighPace 80) from Pfeiffer is placed. This pump needs a prevacuum of 22 mbar for N_2 which can be easily reached by the fore pump. The final pressure for the turbo molecular pump is $5*10^{-10}$ mbar [37]. Figure 17 shows a first vacuum test with the switch-on points of fore pump and TMP. After five hours saturation was observed at a pressure of $2.5*10^{-5}$ mbar. Due to this a leakage was assumed and found at the gas port. By closing this leakage a pressure of $8.2*10^{-9}$ mbar after 116 hours was reached. For reaching a lower pressure in a faster time interval the chamber could be baked out to accelerate desorption of water and organic materials from

the chamber walls [12]. Both pumps are placed on damping pads to save the test setup from vibrations.

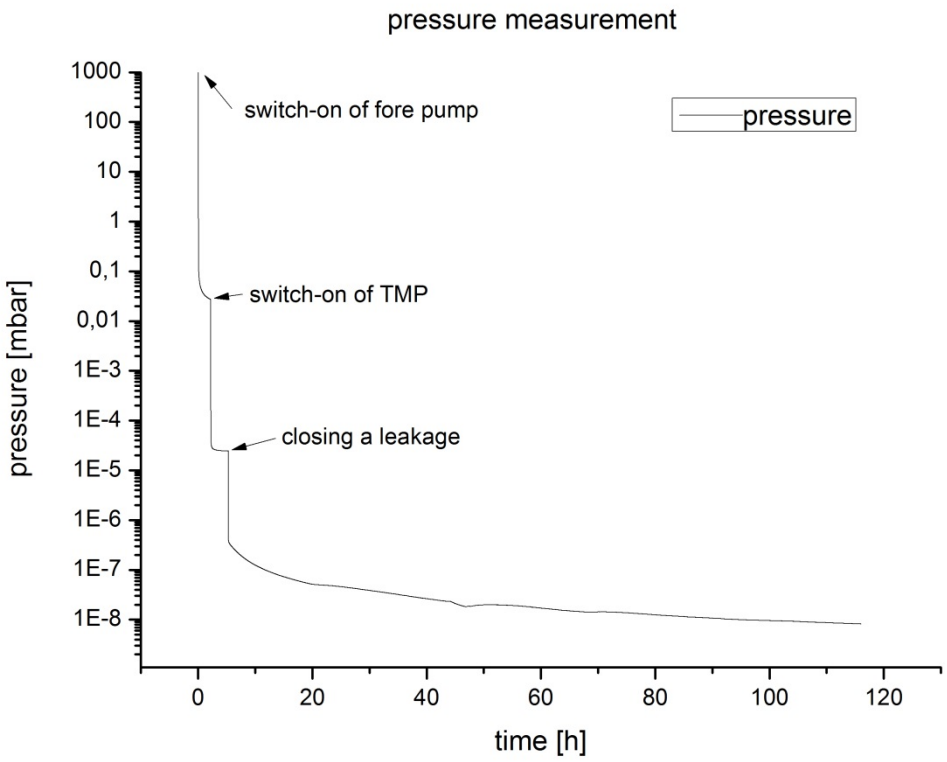

Figure 17: First pressure measurement after vacuum chamber set up.

3.3.3 Vacuum measurement system

The Compact Full Range Gauge PKR 261 from Pfeiffer Vacuum is used for online measurement of pressure in the vacuum chamber. This device is a combination of cold cathode transmitter and Pirani system with an effective range from atmospheric pressure (1000 mbar) to ultra-high vacuum ($5*10^{-9}$ mbar).

3.4 Optical components

3.4.1 Optical beamline

Several mirrors are needed to guide the beam into sample plane. In a first step the laser beam is coupled into the tripler to create UV light. Therefore mirrors with a coating for 1064 nm are used. After tripler the beam is guided by mirrors with a coating for 355 nm. All these mirrors have their highest reflectivity for an incident angle of 45°.

For upcoming tests the beam profile and beam energy have to be characterized. Therefore a small part of the laser beam is coupled out by wedges. The two surfaces of the wedges have a tilt of 3°. The main part of laser beam is transmitted but on both surfaces a small part is reflected. These reflected beams are used for online characterization of laser beam.

3.4.2 Attenuator

The beam characteristics change by varying the output energy of laser. To avoid this, the laser has to run on a constant level. For adjustment of pulse energy respective fluence an attenuator is used. This attenuator consists of a half wave plate and a thin film polarizer, both AR coated for 355 nm. The polarizer is aligned under the Brewster angle in the optical path. This means that perpendicularly polarized light is reflected and parallel polarized light is transmitted. In front of polarizer the wave plate is set. By changing the polarization angle with the wave plate the fluence can be changed.

3.4.3 Beam shaping

The final task is to focus the laser beam onto the sample for investigation of laser induced damages. But the fluence at the entrance window of UHV chamber has to be small and therefore the illuminated area has to be larger. Otherwise damages occur at the entrance window, too.

Therefore two lenses with focal lengths of 500 mm or 750 mm are tested. The lenses generate a small spot at the sample and a larger spot at the entrance window. Table 4 shows the measured values in these positions.

Table 4: Measured values for different focusing lenses

Focusing lens [mm]	Beam diameter @ sample plane [mm]	Beam diameter @ entrance window [mm]
750	0.307	0.5
500	0.173	0.64

The lens with focal length of 500 mm generates a smaller spot and is therefore used in this work. Fluences at the sample plane and at the entrance window are calculated with this values and a measured energy of 500 µJ.

$$\boldsymbol{H_{sample\ plane,45°}} = \frac{2 * E_p}{\pi * \frac{r^2}{\cos(45°)}} = \frac{2 * 500\ \mu J}{\pi * \frac{(86.5\ \mu m)^2}{\cos(45°)}} = \boldsymbol{2.2\ J/cm^2}$$

$$\boldsymbol{H_{entrance\ window,0°}} = \frac{2 * E_p}{\pi * r^2} = \frac{2 * 500\ \mu J}{\pi * (320\ \mu m)^2} = \boldsymbol{0.3\ J/cm^2}$$

The calculation shows that the fluence at sample plane is seven times larger than the fluence at entrance window. This means that fluences which are set in these experiments do not create damages at entrance window of vacuum chamber.

3.5 Evaluation techniques

3.5.1 Insitu technique

For online visualization of damages the long distance microscope QM100 from Questar is used. This special type of microscope allows very large working distances from 15 cm to 35 cm. The QM100 is a Maksutov Cassegrain Catadioptric system (see chapter 2.4.1) and therefore similar to a telescope but used as microscope. [38].

Figure 18: Long distance microscope QM100 from Questar [38]

In case of the working distance, as it set for these experiments a resolution of nearly 1 µm should be reached (see Table 5) [38].

Table 5: Specification for LDM QM100 in dependence on working distance [38]

Working Distance [cm]	Numerical aperture	F-number	Resolution [µm]
33.5	0.83	6.0	10
25.4	0.115	4.3	
15	0.142	3.5	1

In a first step the resolution of images captured with LDM is checked. Therefore a plane plate with a micro benchmark with 10µm distances between two lines is acquired from

LDM in position of used working distance. Due to the fact that the lines are clearly separated the resolution is lower than 10 µm.

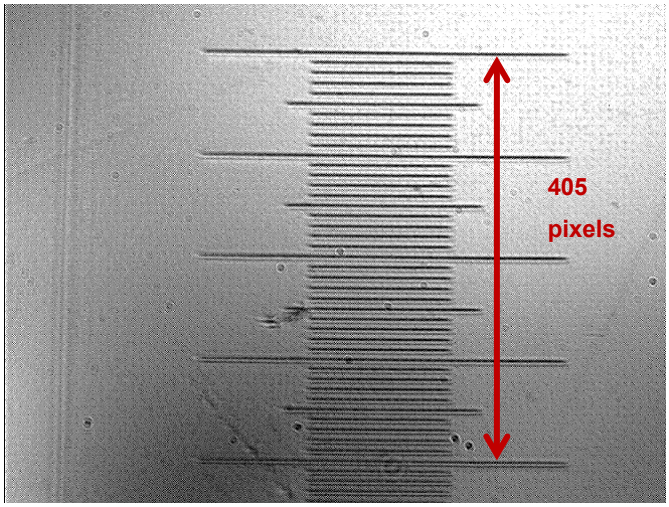

Figure 19: LDM image (658x496 pixels) of micro benchmark with line distance of 10 µm.

Figure 19 shows the image of micro benchmark. The pixel distance of marked arrow is 405 pixels and corresponds to a distance of 400 µm. This results in a calibration value for one pixel to 1 µm.

3.5.2 Exsitu techniques

For a first exsitu investigation a Nomarski microscope from Olympus is used (see Figure 20). The functionality of such a microscope is described in chapter 2.4.2. Objectives with four different magnifications are available (1.25x, 10x, 20x, 50x). [39]

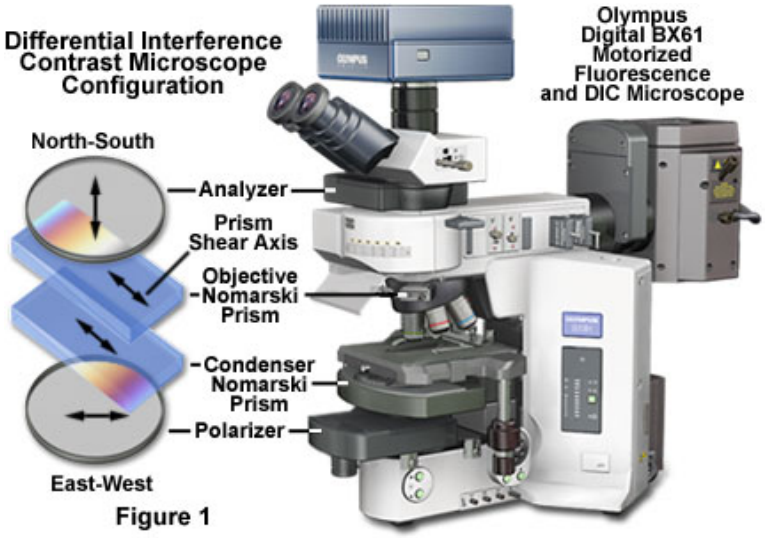

Figure 20: Nomarski microscope digital BX61 from Olympus for DIC microscopy and fluorescence microscopy [39].

In addition to get further information about depths of damages a white light interferometer microscope (WLIM) from Veeco (NT9080) and an atomic force microscope for sample investigation are used.

4 Experimental results

4.1 Basic considerations

All experiments are done with the test bench described above. The parameters for each test are specified in the corresponding chapter. Furthermore any test has the same sequence. After placing the sample in the vacuum chamber, the pumps create a vacuum in the range of 10^{-8} to 10^{-9} mbar. Due to this kind of tests the final pressure is not crucial for results. Directly after start of laser irradiation the long distance microscope takes images from location where laser induced damages should occur. When the test series is completed, the sample is removed from the chamber and investigated with Nomarski microscope. The comparison between the LDM and the Nomarski microscope shows how good the LDM detects the shapes of damage formation.

There are basically two types of coated samples which are investigated. The first sample type has a high-reflective coating for a wavelength of 355 nm and an angle of incidence of 45°. Corresponding test samples are available with IBS or EBE coating. The second sample has an anti-reflective coating also for a wavelength of 355 nm, but an angle of incidence of 0°. However the sample is irradiated under angle of 45° due to observation angle of LDM which is normal to sample surface. This coating is only available with an IBS coating. All coatings are deposited only on front side of fused silica substrates.

The first investigation is a single shot test similar to 1-on-1 test. Therefore damages are created with a single laser pulse with certain fluence. In this experiment high reflective and anti-reflective samples are investigated but only the samples with IBS coating.

A following test series shows the dynamic damage formation and is similar to S-on-1 test whereat the parameter S stands for the total number of pulses which hit the sample at one position. These tests are executed with all three sample combinations to show general differences between the coatings.

The anti-reflective coatings show another damage characteristic compared to the high-reflective samples. This effect is analyzed in a next step. Therefore very small damages (micro pits) are created and investigated on AR samples. A white light interferometer and an atomic force microscope are used to get further information about the morphology of damages.

In a last experiment the influence of laser repetition rate on the LIDT is studied in case of anti-reflective IBS coatings.

During the experiments some testing components are changed or optimized which is described in chapter 5. But parameters just changed between the test series and not between single tests. This means that only the results of a certain test series can be compared to each other.

4.2 1-on-1 tests

This chapter deals with single shot tests which show the range around the damage threshold for specific type of coating. This test also should verify the resolution limits of LDM which are declared in chapter 3.5.1. Tested are IBS coatings for HR and AR applications.

The measured high-reflective coating has an expected value for LIDT of 11 J/cm² for 10k shots and 18.8 J/cm² for single shot tests which was measured by scattered light detection in former work. But by this method only damages with dimensions more than 10 µm can be detected online.

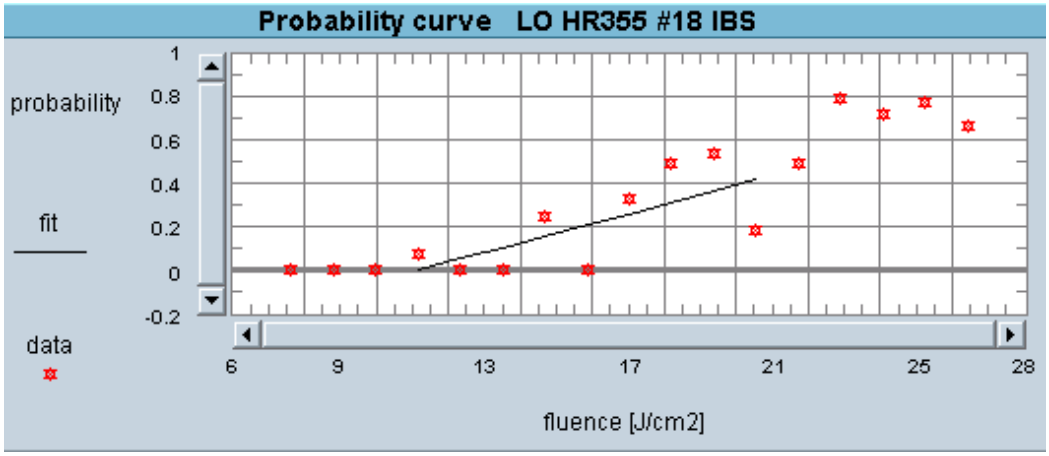

Figure 21: Probability curve for HR355nm IBS, sample number #18, plotted is damage probability over fluence in J/cm² (for 10000 total pulses), red dots are the data points, the crossing point of fitting curve and x-axis gives the LIDT value. [40]

Figure 22 shows the results of 1-on-1 tests at high reflective samples with fluence in the range from 8 J/cm² to 12 J/cm². The image pairs are split in a Nomarski image (left hand side) and the insitu image from long distance microscope (right hand side). Each LDM

image is corrected by a corresponding background image for compensating artefacts from imaging.

By means of LDM damages down to a size of nearly 3 µm can be detected online. This makes the damage detection more sensitive for smaller damages than scattered light detection. Another point which can be seen in this example is the statistical factor in the region of damage threshold. So a small damage occurs at 8 J/cm² (Figure 22a), but a second test at 9 J/cm² (Figure 22b) does not create damage. This can be explained by Figure 21. At lower fluence no damages occur whereas at higher fluence damage occurs each time. But in between these two regions at a specific fluence damages could occur or not depending mainly on material inhomogeneity. [41]

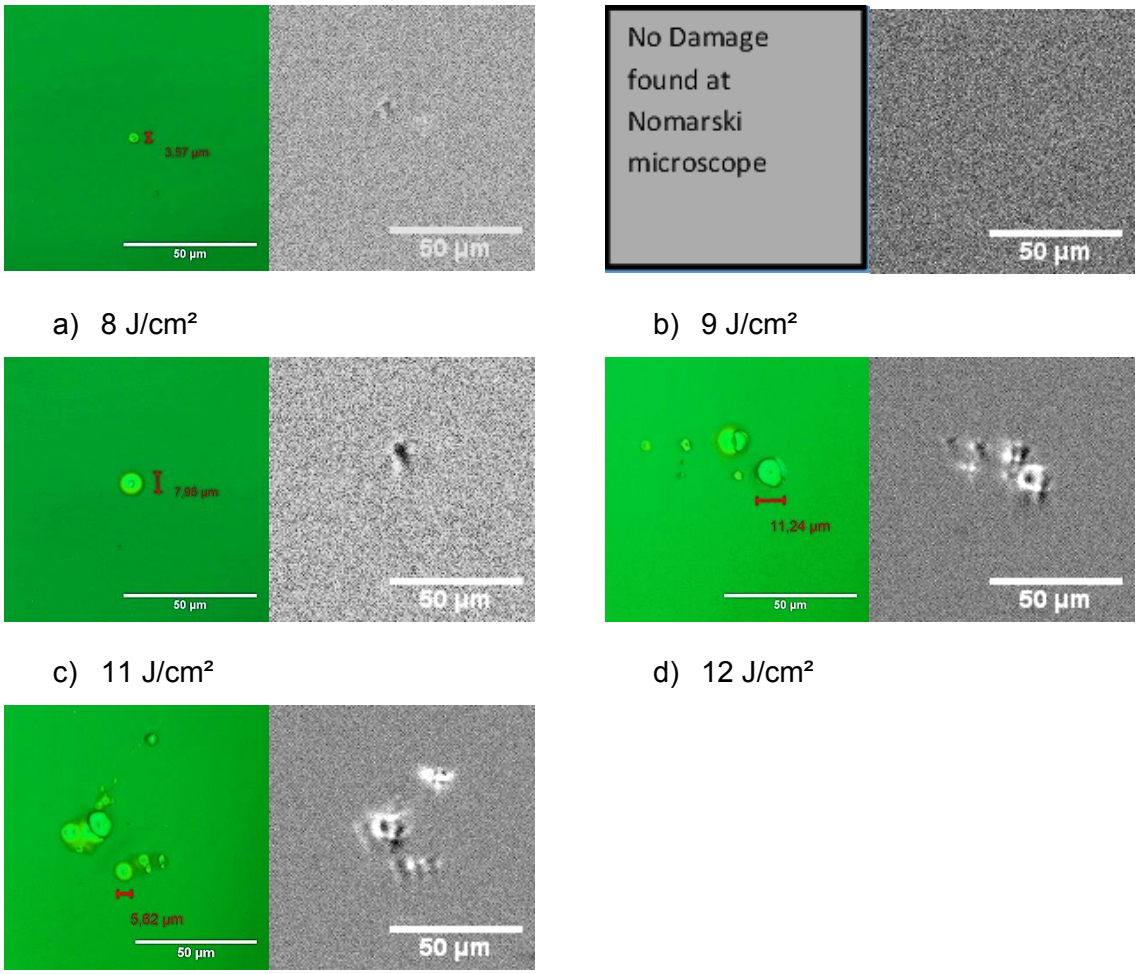

a) 8 J/cm²

b) 9 J/cm²

c) 11 J/cm²

d) 12 J/cm²

e) 12 J/cm²

Figure 22: Nomarski and LDM images of HR IBS samples for single shot tests.

For higher fluences more than one micro pit is created within the beam diameter. The distribution of micro pits can be seen very well.

It has to be mentioned that LDM images are rescaled by software. This means that the dynamic range of each image is optimized to get best possible contrast.

For anti-reflective coatings the expected damage threshold is even smaller in the range of 3.5 J/cm² for 10k shots and 9.7 J/cm² for single shots at this sample (see Figure 23). Also the range between no damage and 100% damage probability is much smaller as at high reflective samples.

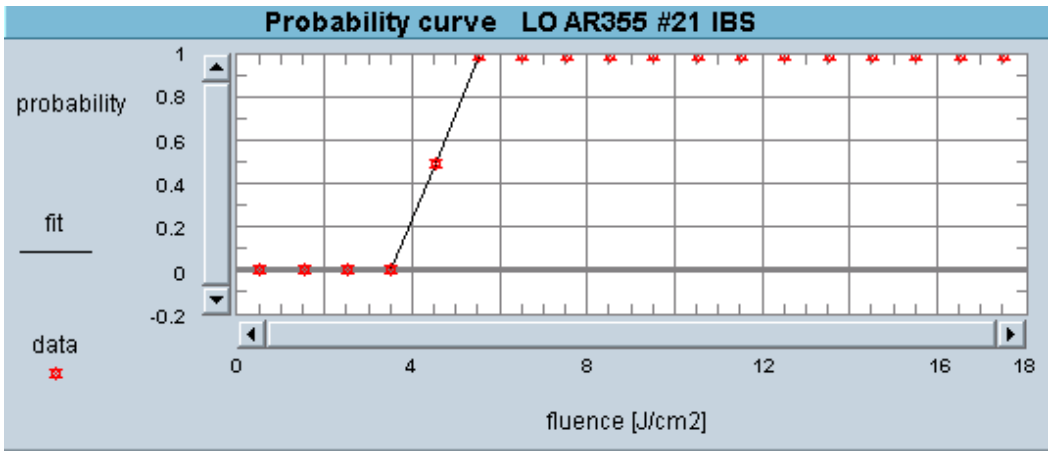

Figure 23: Probability curve for AR355nm IBS, sample number #21, plotted is damage probability over fluence in J/cm² (10000 total pulses), red dots are the data points, the crossing point of fitting curve and x-axis gives the LIDT value. [42]

At high reflective coatings smaller damages (micro pits, 3-5 µm) with long distance microscopy compared to scattered light measurement can be detected. On AR samples also micro pits appear but the single size of one pit is in the range of 1-2 µm which is therefore in the range of resolution limit of LDM. Another point, compared to HR samples is that there are much more micro pits within the beam diameter but due to the small size of single micro pit it is much harder to see a characteristical damage shape at AR samples. It is more like the light scattering at those pits which is detected at LDM. For higher fluences the micro pits create a much bigger damage as Figure 24d shows.

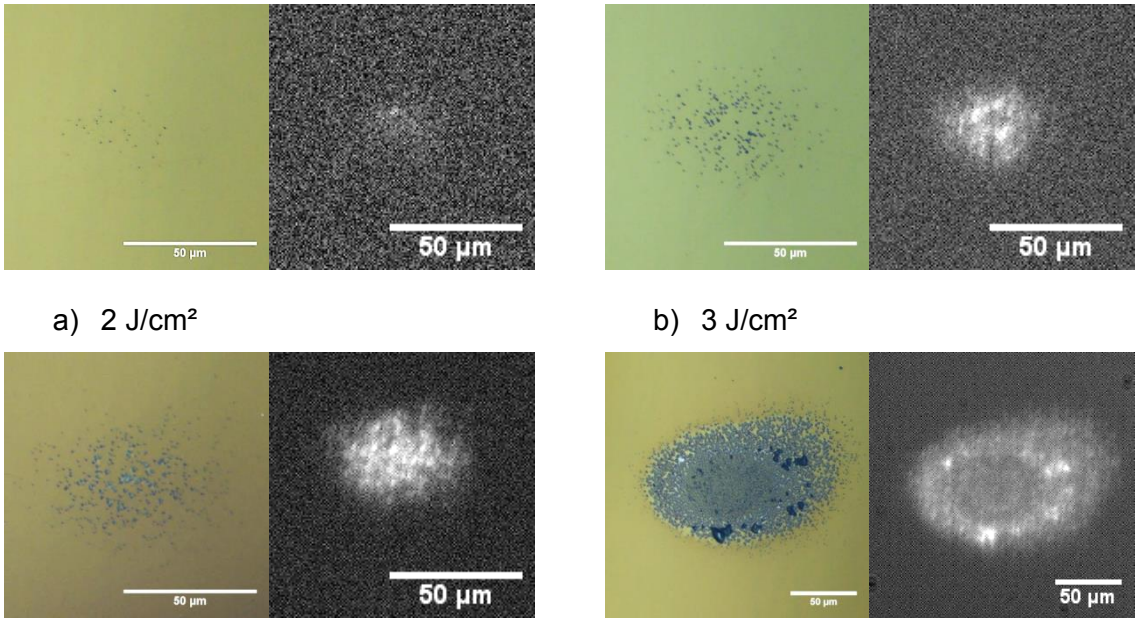

a) 2 J/cm²

b) 3 J/cm²

c) 4 J/cm²

d) 13 J/cm²

Figure 24: Nomarski and LDM images of AR IBS samples for single shot tests.

4.3 S-on-1 tests

This chapter shows results of tests similar to S-on-1 tests which are specified in ISO 21254 [5]. According to this standard the S-on-1 method is a multi-shot test on one position whereat the S characterizes the total number of pulses which hit the sample finally. Those experiments are realized with high reflective samples coated with IBS and EBE. Also the antireflective sample is investigated but only with IBS coating.

4.3.1 Evaluation method for S-on-1 tests

In this section a short introduction is given for better understanding of results and their illustration.

The highest acquisition rate for Andor camera is 30Hz but the regeneration time of 0.8 ms for flash light reduces the final testing velocity to 1Hz. Therefore all tests in this section are realized with laser frequency of also 1Hz at which an image after each laser pulse can be recorded.

The example in Figure 25 shows the damage formation on high reflective IBS coating for a fluence of 7 J/cm² and pulse number of 50. It can be seen that damage starts with first

pulse and grows rapidly until a pulse number of 35 is reached. For higher pulse numbers up to 50 pulses no further lateral growth can be seen because damage diameter converges to beam diameter.

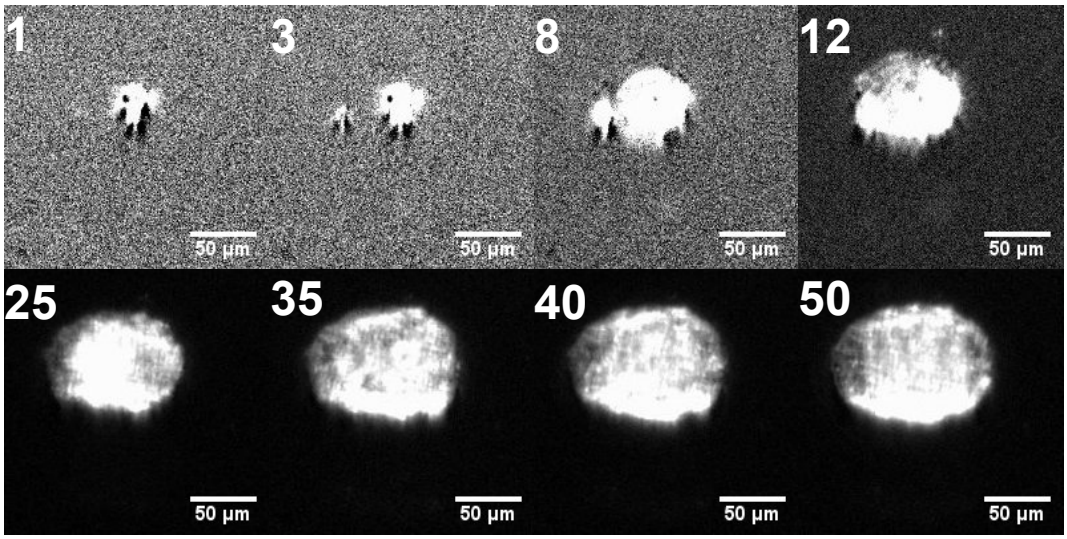

Figure 25: LDM images damage formation of IBS HR coating at 7 J/cm² and total pulse number of 50.

After damage tests all images are background corrected using Andor camera software. Therefore a background image was acquired from the same sample position before laser irradiation. Background corrected images are saved into tif format.

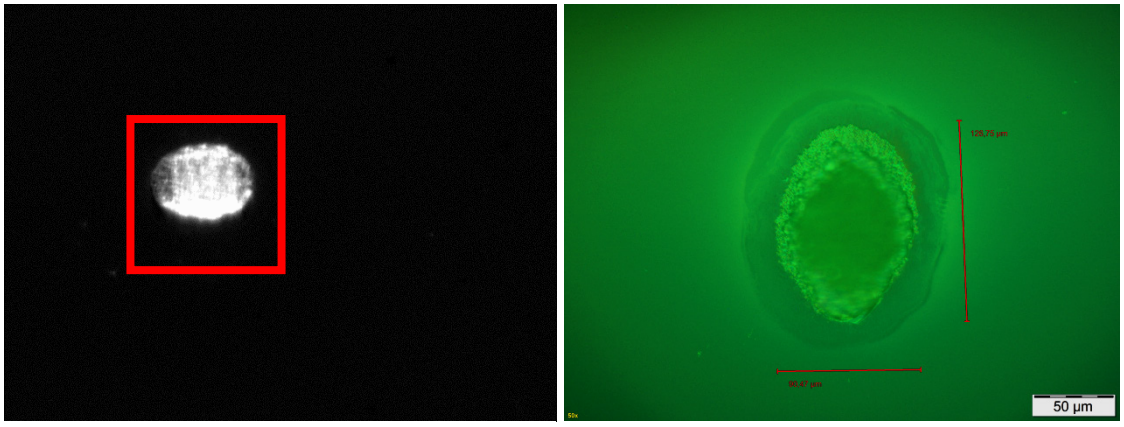

Figure 26: Single image from IBS HR test at 7 J/cm² and 50 pulses with region of interest (red square)(left), Nomarski image of laser induced damage (shifted by 90° due to investigating direction)(right).

Next step is realized with Wolfram Mathematica 10.0. This program cuts out a certain region of interest (ROI) as it is defined in Figure 26. Then the program adds up the gray scale values for all pixels inside the ROI. Finally each image got a specific value which is depending on damage dimensions.

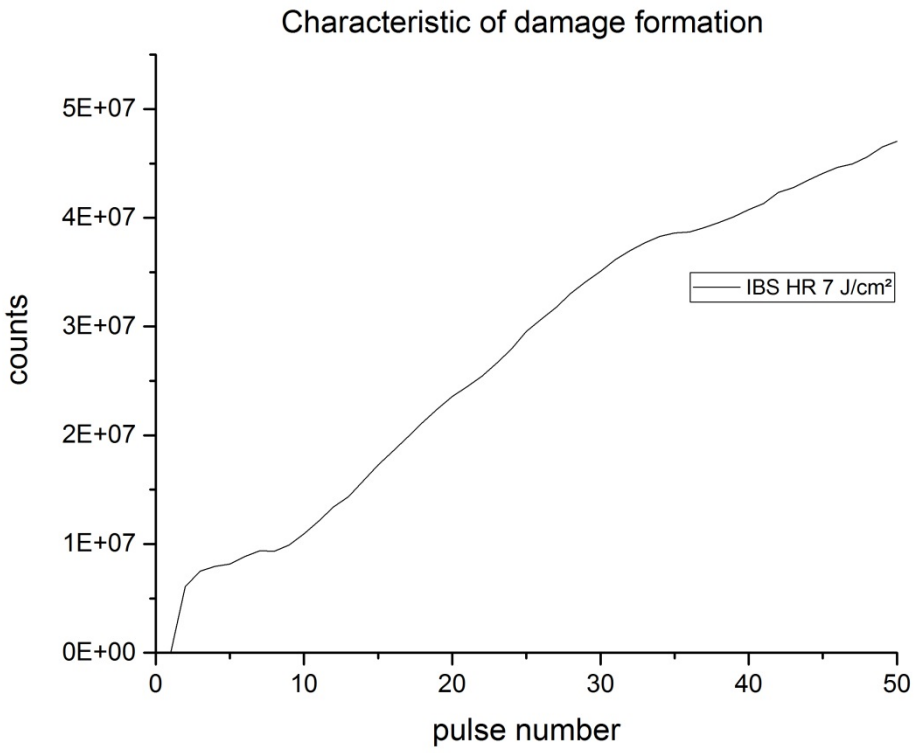

Figure 27: Characteristic of damage formation for HR IBS coating for 7 J/cm² and pulse numbers from 1 to 50 pulses, background corrected counts on ordinate.

In Figure 27 the characteristic of damage formation for the upper example is displayed with pulse number at abscissa and the corrected count number at ordinate. The step at the beginning shows the origin of small damage. The rapid damage growth starts at pulse 8 and ends at a pulse number of 35. After 35 pulses such a large damage size is reached that the difference compared to damage size at 50 pulses is insignificant. This can be seen in a small change of slope. All in all Figure 27 shows the characteristic of damage formation and can be used for comparison.

4.3.2 Investigation of HR coatings

The following tests are realized to show the functionality of test bench and to investigate the damage formation of different types of coatings. Therefore two high reflective coatings are investigated.

First one is coated with ion beam sputtering which generates nearly homogeneous layers with a very low rate of failures inside the coating as discussed in chapter 2.5. Figure 28 shows the comparison between four tests with different fluences for high reflective IBS coating. For the test at 6.2 J/cm² no damage and no change of the surface was observable (Figure 28 blue curve). For the tests at higher fluences small damages with dimensions of 3-10 µm occur at the first pulses and grow rapidly with each pulse until a pulse number of 30 is reached. When damage diameter converges to beam diameter the lateral growth is reduced. From these tests the damage threshold for this sample can be estimated to be between 6.2 J/cm² and 6.5 J/cm² for 100 shots.

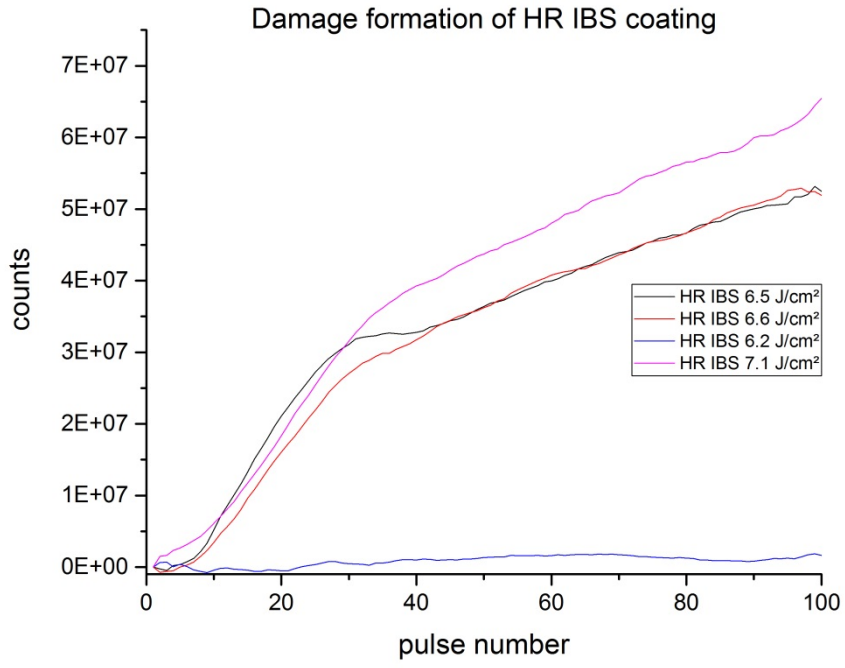

Figure 28: Damage formation of HR IBS coating at different fluences from 1 to 100 pulses, background corrected counts on ordinate.

The second investigated coating is also a high reflective one but deposited with electron beam evaporation (EBE). As expected the damage threshold is lower (3.4 J/cm² to 3.6 J/cm²) compared to IBS coating. But the damage formation has nearly same slope as

IBS coating. Within the first pulses small damages occur and grow rapidly until a pulse number of 30 is reached. After 30 pulses the lateral growth is reduced like in the IBS HR tests before. Probably the damage depth is increasing after 30 pulses and this could be reason for lower light scattering. Finally the image becomes darker and the curve in Figure 29 is decreasing after 30 pulses.

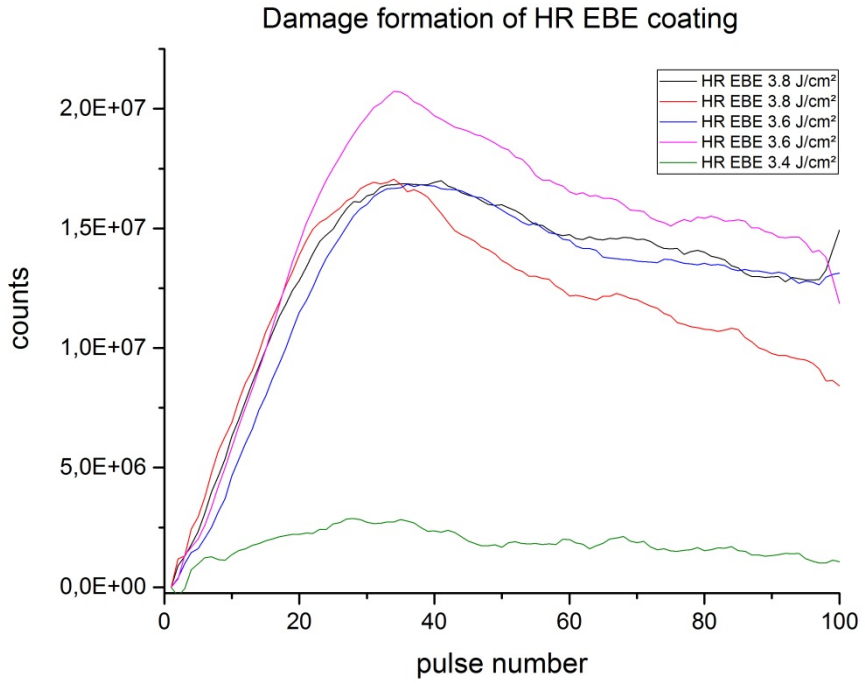

Figure 29: Damage formation of HR EBE coating at different fluences from 1 to 100 pulses, background corrected counts on ordinate.

For better visualization the damage formation for HR IBS coating at 6.6 J/cm² is displayed in Figure 30. Most important steps of damage formation are shown and can be allocated with the pulse numbers (white) to black curve in Figure 33.

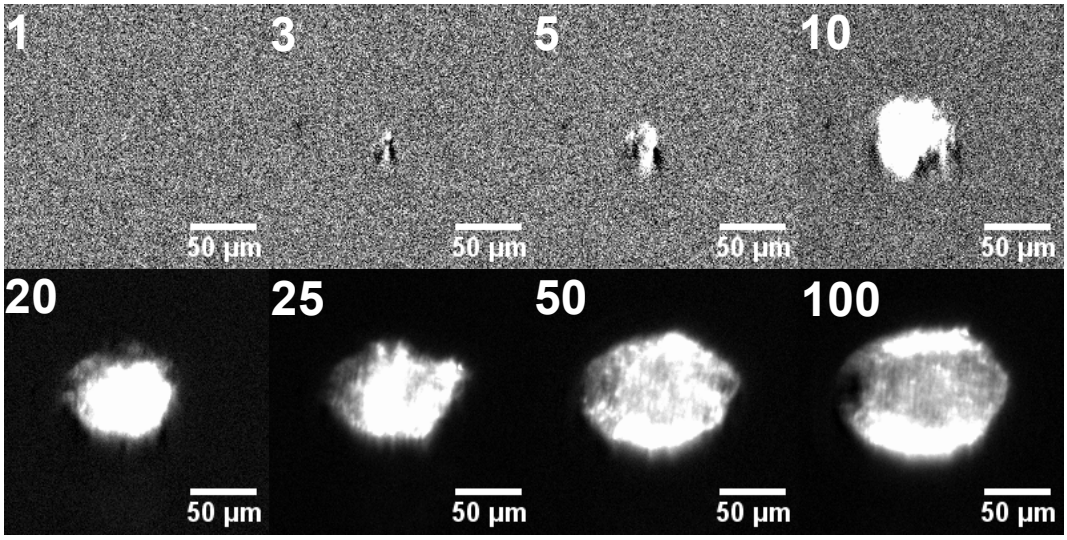

Figure 30: LDM images for damage formation of IBS HR coating at 6.6 J/cm² and total pulse number of 100.

The damage formation for HR EBE coating at 3.8 J/cm² is displayed in Figure 31. The steps of LDM images are the same as at HR IBS example for comparison. The complete trend over 100 pulses can be seen in Figure 33 (red curve).

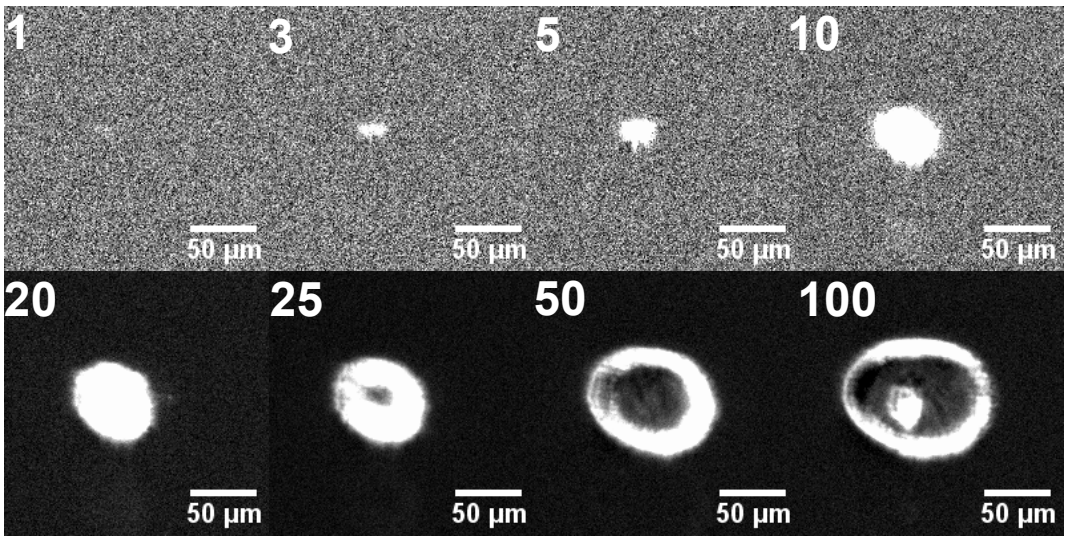

Figure 31: LDM images damage formation of EBE HR coating at 3.8 J/cm² and total pulse number of 100.

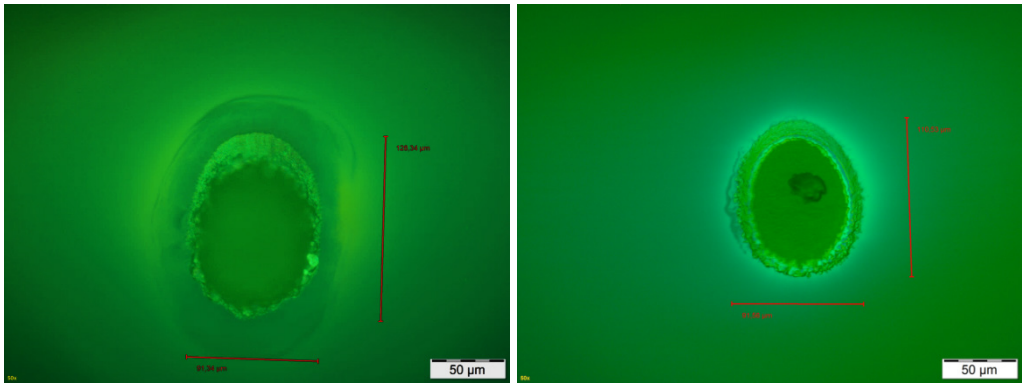

Figure 32: Nomarski images from damages of compared coating types, IBS (left) and EBE (right).

For both samples damage starts with first pulse. When the damaging process starts the rise at IBS seems to be steeper than the rise at EBE coating. For better statements at this phenomenon much more tests are needed. Therefore it is necessary to keep in mind that the laser induced damage threshold for both coating types are far apart from each other. All in all both have their own characteristical growth and can be distinguished from each other.

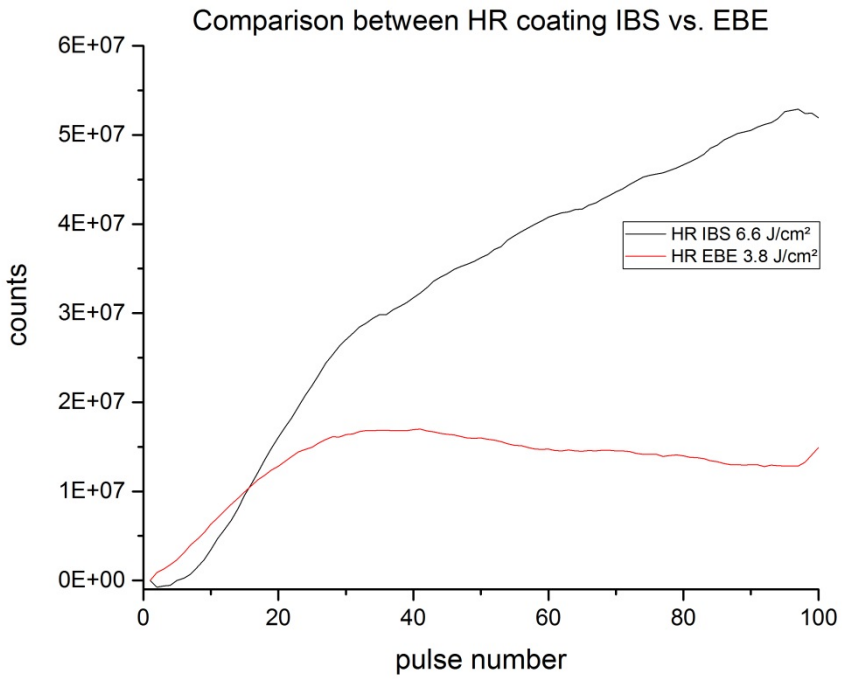

Figure 33: Comparison of damage formations between HR IBS at 6.6 J/cm² and HR EBE at 3.8 J/cm² from 1 to 100 pulses, background corrected counts on ordinate.

4.3.3 Comparable investigation of AR and HR coatings

This chapter compares antireflective and high reflective coatings which are both coated with IBS. The laser induced threshold for AR IBS is lower than 1.9 J/cm². At Figure 34 three tests for AR IBS coatings are displayed. For tested fluences micro pits are created with first pulse. For higher fluences (3.3 J/cm² and 4 J/cm²) the corresponding LDM images have a higher count rate wherefore two possible reasons exist. On the one hand the region where micro pits occur could be bigger. On the other hand the micro pits could be bigger in detail. These effects declare the higher count rates. After 20 pulses no further growth is detected during the residual 100 pulses for all tests.

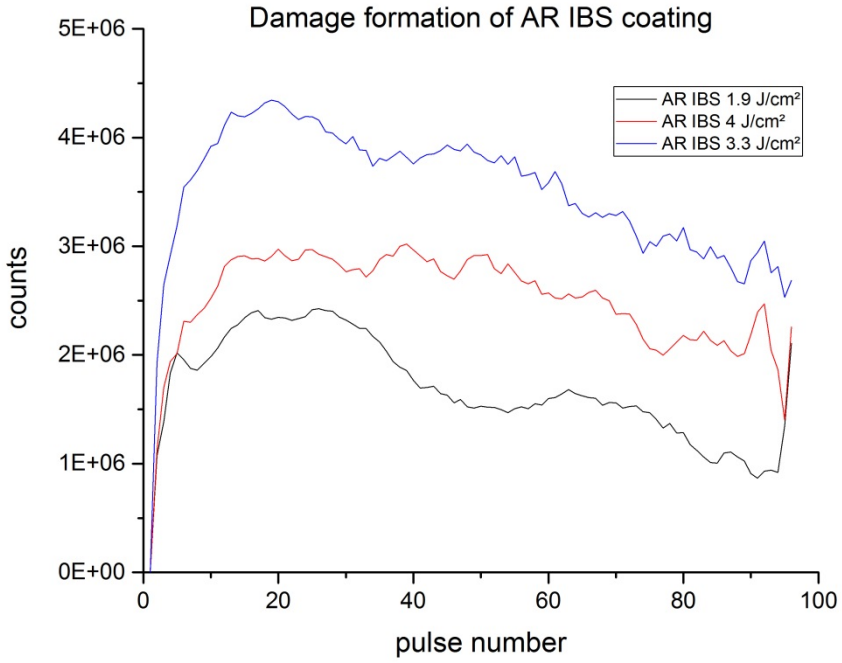

Figure 34: Damage formation of AR IBS coating at different fluences from 1 to 100 pulses, background corrected counts on ordinate.

For comparison the results for HR IBS coating, discussed in chapter 4.3.2 are used. In this section the example at 6.5 J/cm² is compared to AR IBS coating. The HR coating behaves as described in the upper chapter. Small damage occurs with first pulses and grows until size of beam diameter is reached.

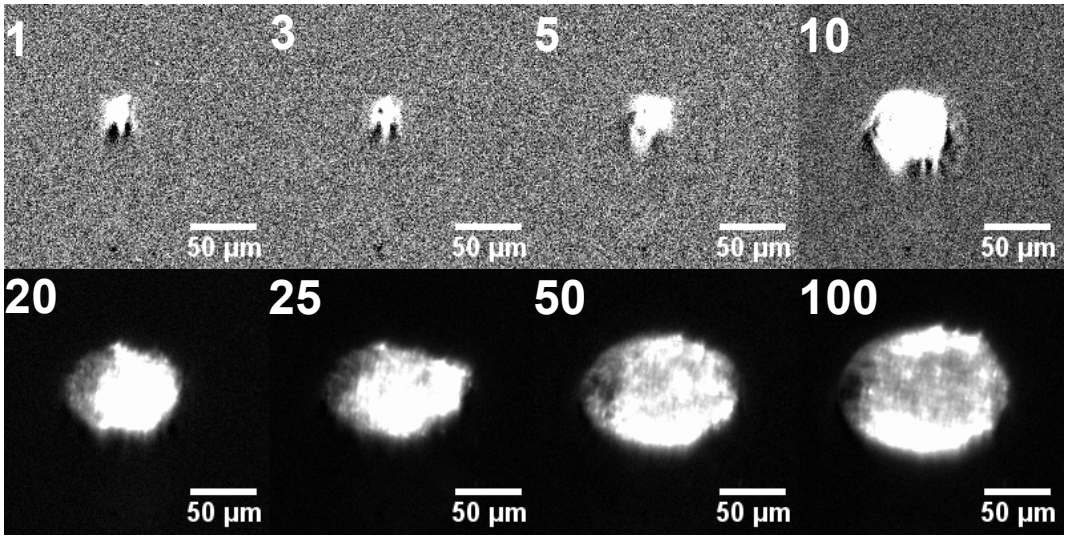

Figure 35: LDM images for damage formation of IBS HR coating at 6.5 J/cm² and total pulse number of 100.

Figure 36 shows selected steps in damage formation of AR IBS coating. It can be seen that a bright area is created with first pulse. Further investigations with Nomarski microscope showed that micro pits were formed (see Figure 37 left). These small damages scatter the light from flash lamp which generates this appearance. In addition no growing process can be detected in contrast to HR coatings. However the micro pits grow with each single pulse until pulse number 10 is reached. Then they remain constant for residual test.

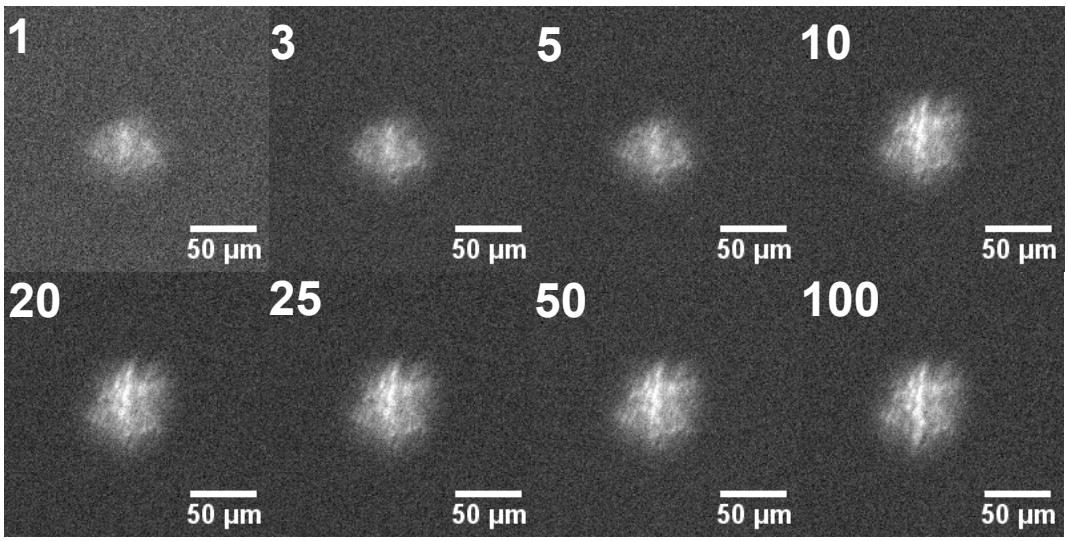

Figure 36: LDM images for damage formation of IBS AR coating at 3.3 J/cm² and total pulse number of 100.

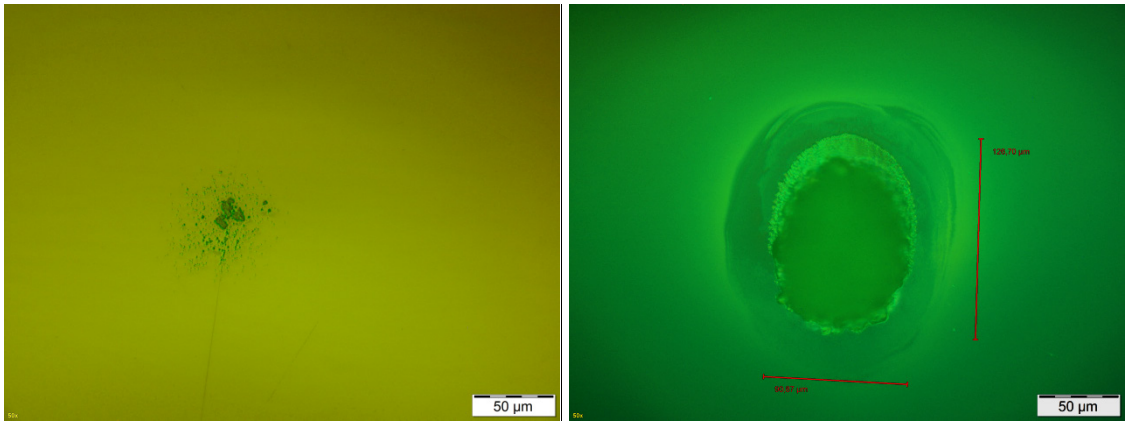

Figure 37: Nomarski images from damages of compared IBS coatings, AR wit 3.3 J/cm² (left) and HR 6.5 J/cm² (right) after 100 shots.

Figure 37 shows Nomarski images of damages on AR coating (left) and HR coating (right) but with different fluences. Damage at HR sample is much bigger and at AR micro pits can be seen which already start to grow together.

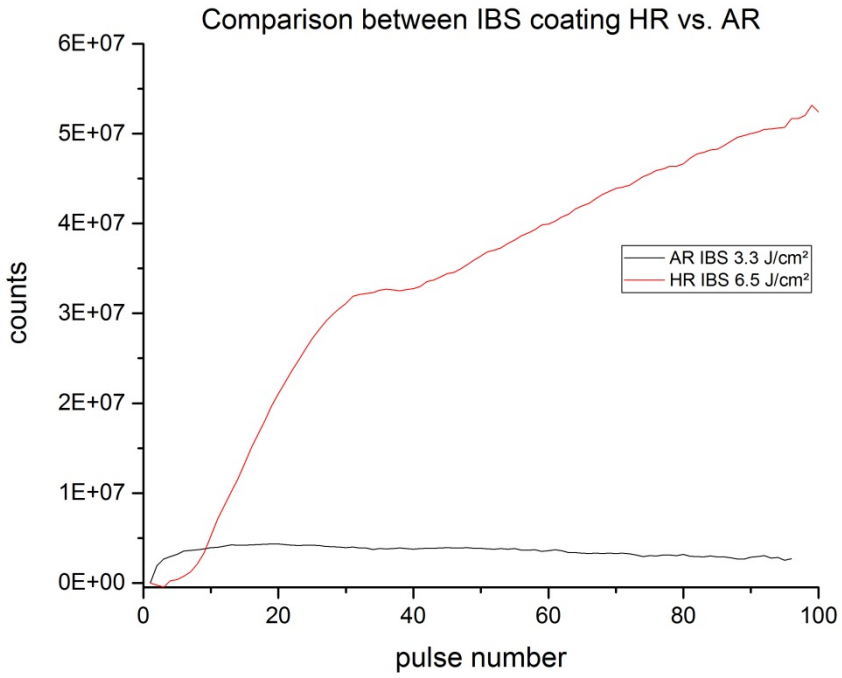

Figure 38: Comparison of damage formations between HR IBS at 6.5 J/cm² and AR IBS at 3.3 J/cm² from 1 to 100 pulses, background corrected counts on ordinate.

Comparing the curves in Figure 38 the statement can be done that AR coating reaches a constant level at which no further damages occur within the 100 pulses. At HR coating the

damage diameter is growing until 100 pulses hit the sample. At AR sample damages occur earlier and fewer pulses are needed before the saturated part is achieved. Whereas HR coatings show a damaging process over 100 pulses. But it should be noted, that the comparability is limited because the applied fluences were different.

The main result of this experiment is that it could be worth to spend more time on the investigation of these micro pits. It is quite interesting to answer questions about the characteristics and the damage formation of micro pits at AR IBS coatings.

4.4 Investigation of micro pits

Micro pits are defined as small damages with sizes in the micron range. One major task of this thesis is the investigation of dynamics of damage formation of micro pits at antireflective IBS coatings. But before corresponding tests can be realized, the nature of micro pits has to be understood.

Therefore the characteristics of micro pits are discussed in the following. The following tests are no more comparable to prior results because illumination for image acquisition is changed which is described in chapter 5.

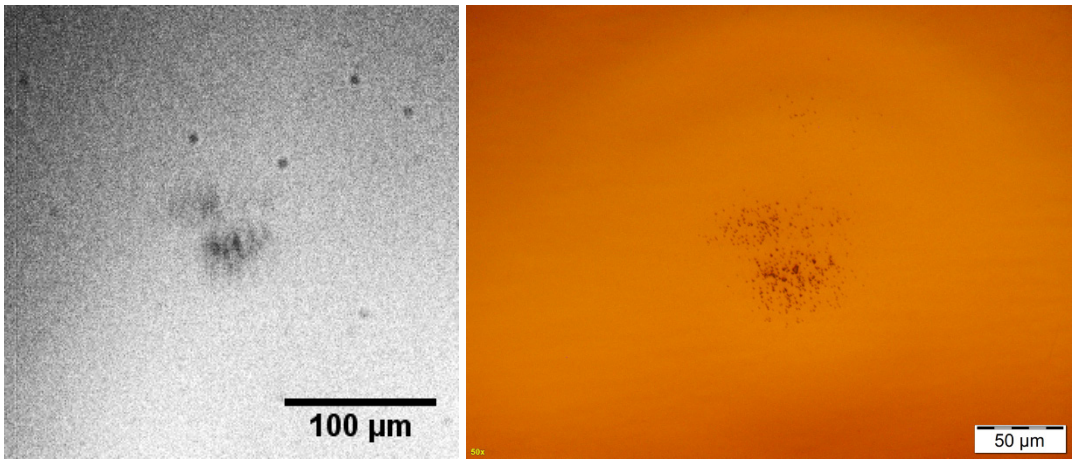

Figure 39: Characteristic shape of micro pits at AR IBS coating after 10000 pulses with 100Hz repetition rate, LDM image (left) and Nomarski image (right) for comparison.

Micro pits appear at AR IBS layers on the front surface. This can be concluded from the topographies measured with WLIM and AFM. These profiles show that the micro pits are

growing from the top side into the layer. The Nomarski image in Figure 39 shows a typical laser induced damage with micro pits.

A lot of different sized pits have formed in the region of laser footprint. The complete shape of all micro pits can be seen quite well in online investigation with long distance microscope. But the resolution of exsitu microscopy cannot be reached.

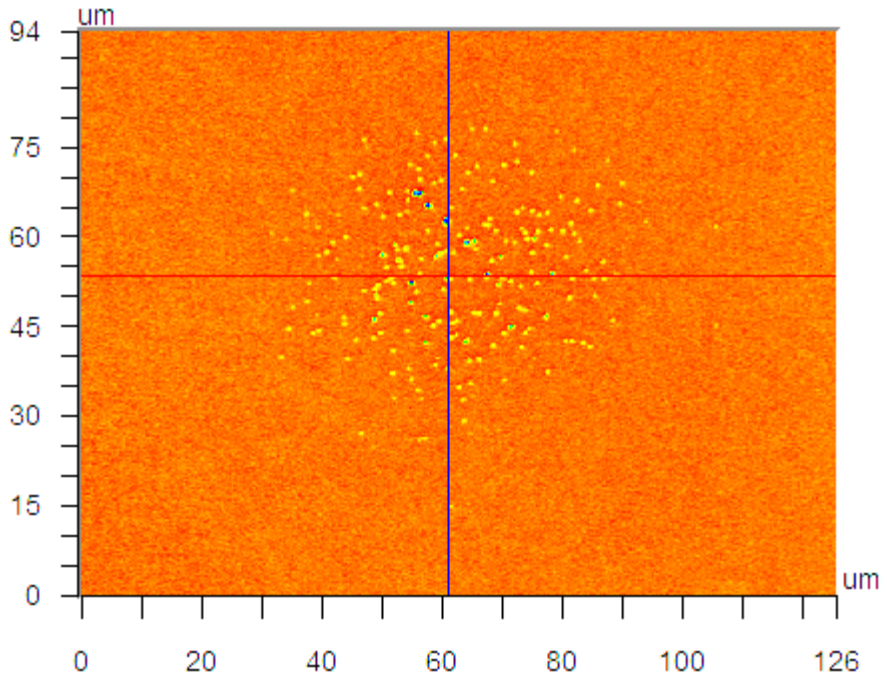

Figure 40: 2-dimensional image of micro pits at AR IBS coating measured with white light interferometer Veeco (NT9080), with marked profiles in x- and y-direction.

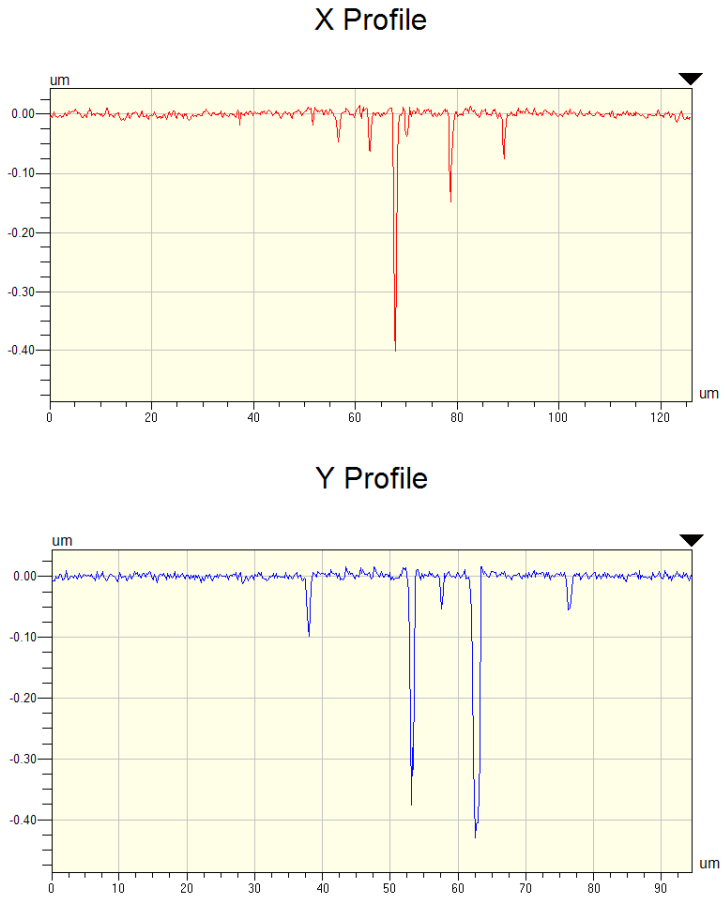

Figure 41: X- and y-profile of 2-dimensional image of micro pits at AR IBS coating measured with WLIM Veeco (NT9080).

For further investigation it is important to get information about the dimensions of single micro pits. Therefore white light interferometry is used. The micro pits measured with WLIM are displayed in Figure 40. It shows another position on sample but same coating type.

The diameter of a single micro pit varies between 1 and 4 µm and the depth is in the range of 50-400 nm.

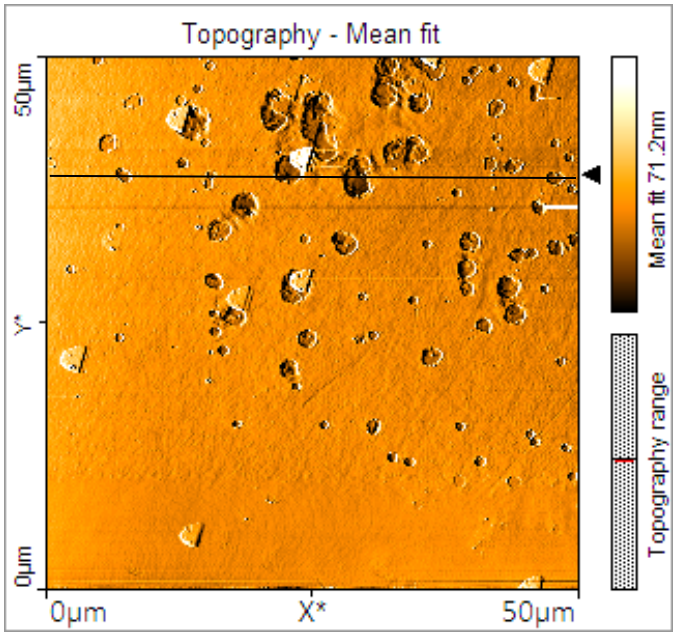

Figure 42: 2-dimensional image from atomic force microscope of micro pits at AR IBS coating, line marks position which is used for topography.

In a further investigation of micro pits with atomic force microscopy at another sample position even smaller depth of micro pits can be measured (see Figure 43). The main advantage of AFM as already described is the higher resolution compared to WLIM. Figure 42 shows a 2-dimensional image from AFM of micro pits which shows the dimensions of the micro pits.

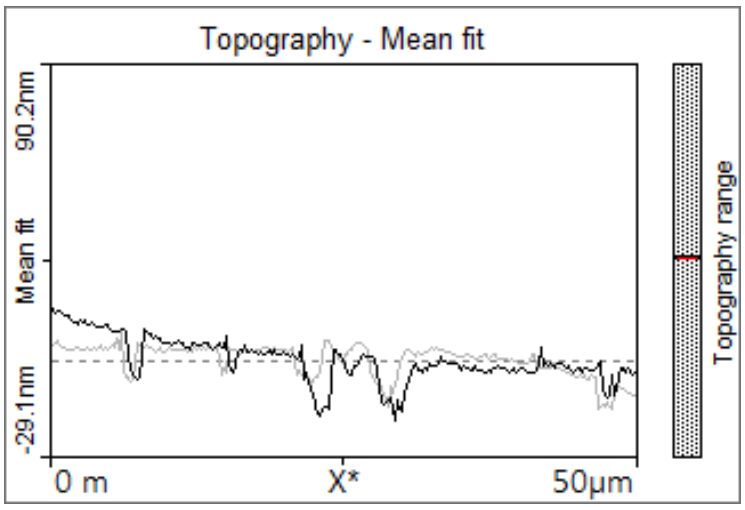

Figure 43: Topography of image from atomic force microscope of micro pits at AR IBS coating.

After this introducing remarks further tests are described for detailed investigation of micro pit formation. Therefore an IBS AR sample is irradiated with a fluence of 5.5 J/cm² and 100Hz repetition rate. The total number of pulses per position was 10000. The image acquisition is realized with 10Hz which results in 1000 images. Figure 44 shows the accumulated gray scale intensity in a defined region of interest in dependence on pulse number.

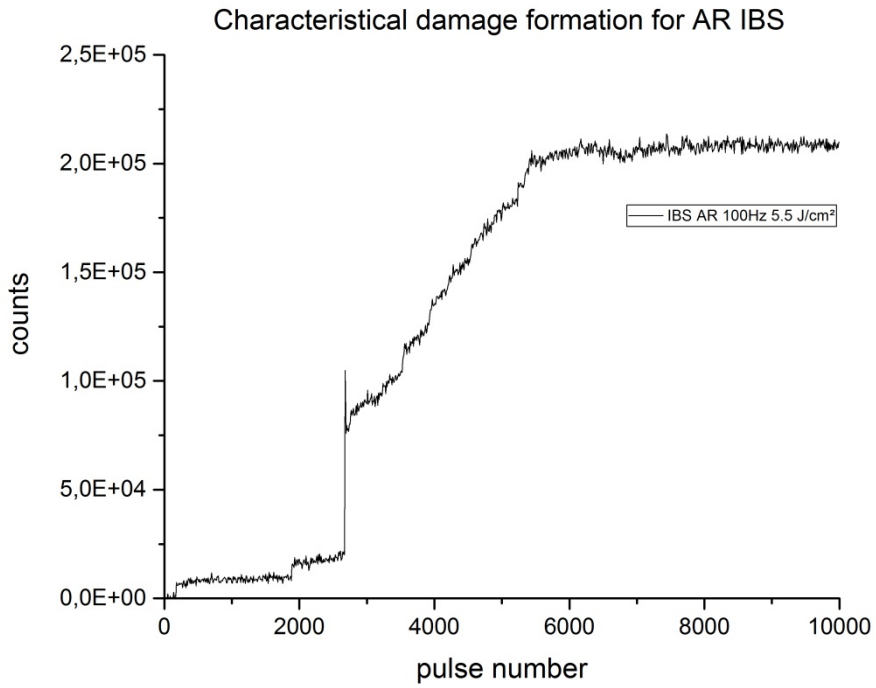

Figure 44: Characteristical damage formation for AR IBS coating for 100Hz, 5.5 J/cm² and 10000 pulses, background corrected counts on ordinate.

The graph shows several steps at pulse numbers of 190, 1900 and 2700. Compared to Figure 45 at pulse 190 and 1900 few micro pits occur which can be resolved hardly. But at pulse 2700 bigger micro pits occur which can be seen at the high step in the graph. These steps at single pulses can be explained by the stronger energy absorption at micro absorbers (inhomogeneity, impurities, etc.) in the layer compared to homogeneous layer sections. [6] The slow increase can be explained by micro pits growing together which is the case when absorption at created micro pits increases over a specific limit.

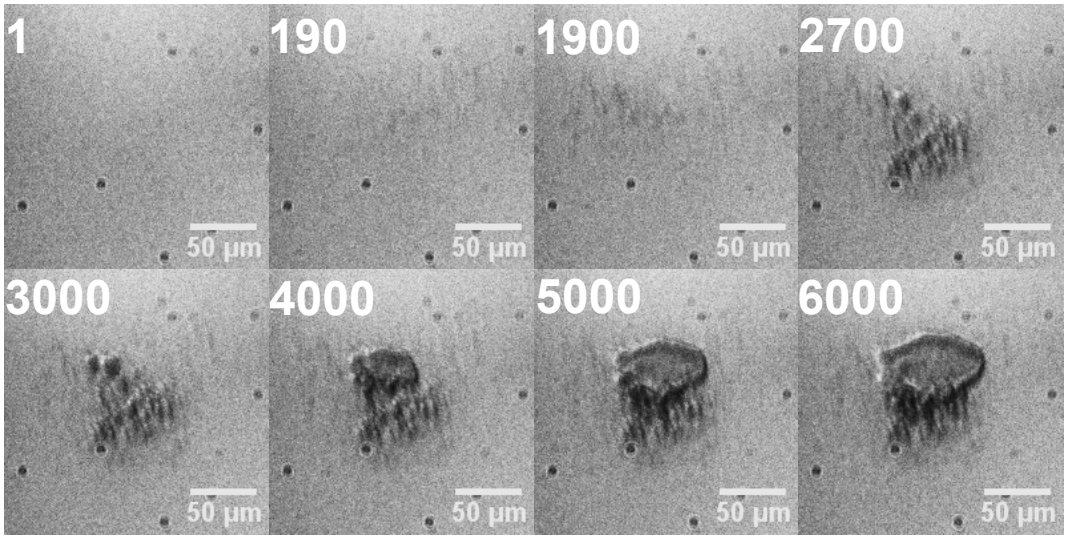

Figure 45: LDM images of damage formation of AR IBS coating; 5.5 J/cm², 100Hz.

Figure 46 shows comparison of LDM and Nomarski images of upper example after 10000 pulses.

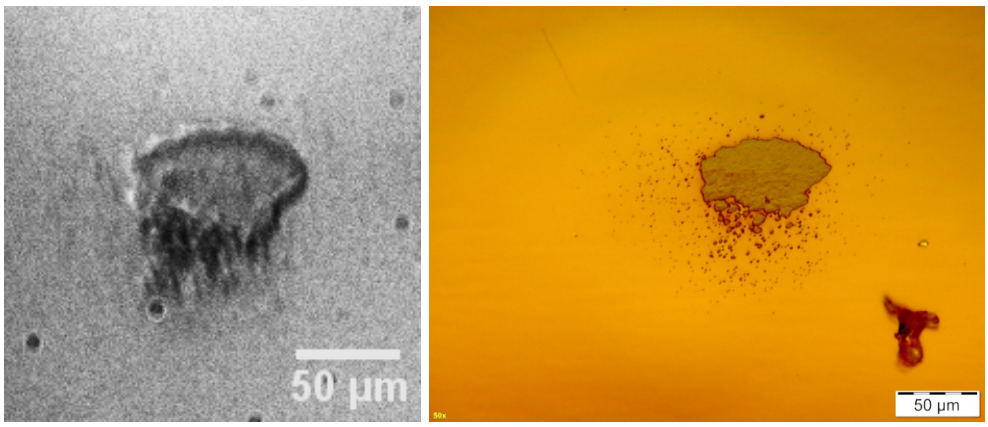

Figure 46: Damage after 10000 pulses of LDM (left) and Nomarski microscope (right) at AR IBS coating (100Hz 5.5 J/cm²).

The final statement is that micro pits occur with single pulses. When a specific limit is reached, this micro pits start to grow together to a bigger damage.

4.5 Dependency of laser repetition rate on LIDT

On the basis of absorption a faster repetition rate should induce damages at fewer pulses because irradiated material has less time to regenerate or to transfer the heat produced by laser beam. Therefore in this chapter the dependency of laser repetition rate on LIDT for IBS AR coating is investigated.

As repetition rates 20Hz and 100Hz are chosen. Based on the fact that illumination is optimized the maximum acquiring frequency of 30 Hz of the camera is limiting the investigation rate. First tests should acquire images after each pulse. This is why 20Hz is chosen for the lower limit. As upper limit the highest adjustable laser rate of 100Hz is used. Each test consists of a total pulse number of 10000 pulses. Due to the fact that the camera software only can handle with data sets of maximum 1000 images, the acquisition rate is set to 10Hz. This results in a temporal resolution of 10 pulses between two successive images.

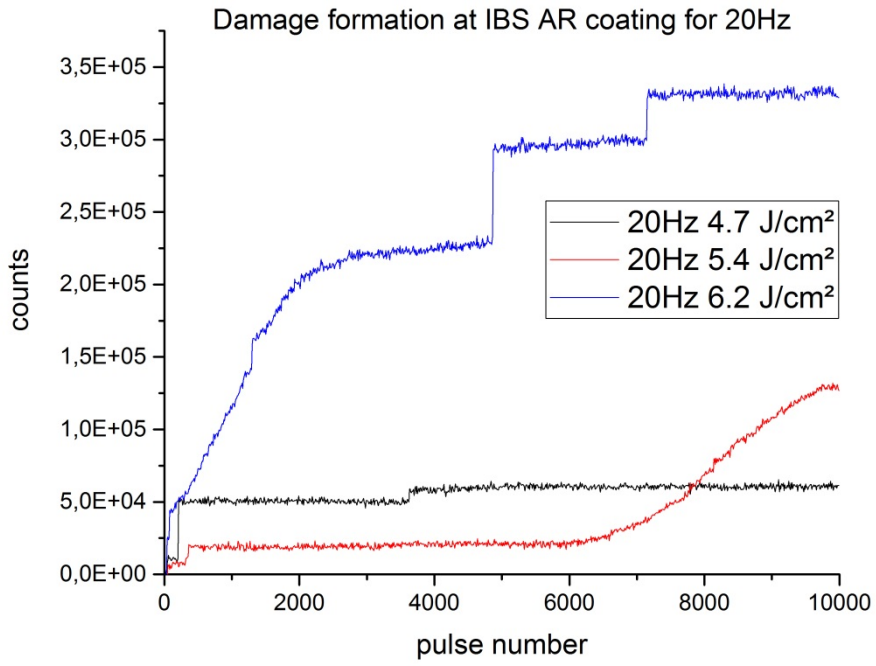

Figure 47: Damage formation at IBS AR coating for 20Hz laser rate, 10000 pulses and different fluences, background corrected counts on ordinate.

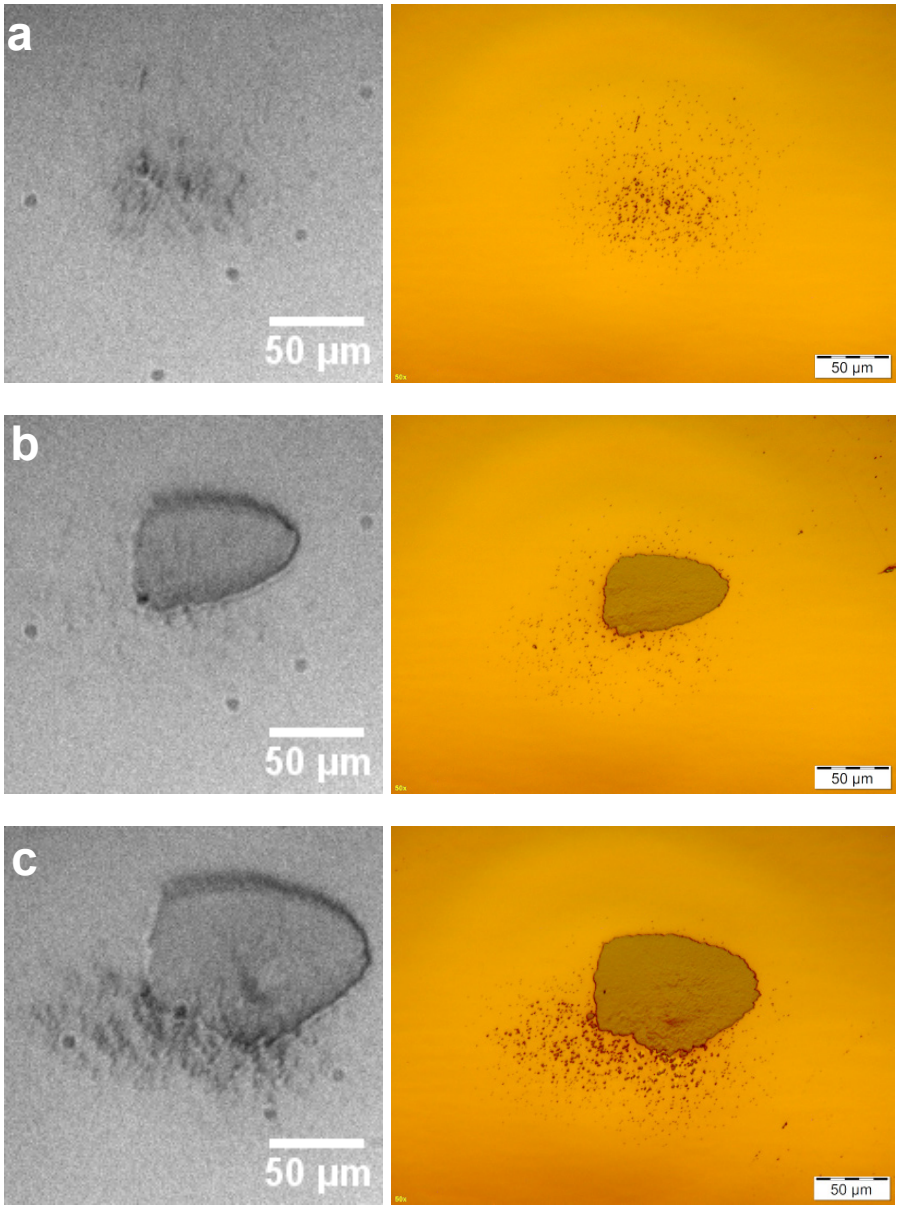

Figure 48: Comparison between LDM (left) and Nomarski images (right) at different fluences for 20Hz tests: a) 4.7 J/cm² b) 5.4 J/cm² c) 6.2 J/cm².

Figure 47 shows the damage formation at IBS AR coating for a laser repetition rate of 20Hz. For fluence of 4.7 J/cm² only micro pits occur which can be identified with characteristical steps. For 5.4 J/cm² two fast steps in the beginning can be seen and after 6000 pulses a slope distinguish the merging of micro pits. At 6.2 J/cm² also micro pits in the beginning can be detected followed by fast slope. The two steps after the rise are micro pits beside the main damage at the edge of the laser footprint. This example shows that the moment at which micro pits grow together happen with fewer pulses for higher fluences. For much lower fluences only micro pits occur which do not grow together within

10k shots. For better visualization the corresponding LDM and Nomarski images are displayed in Figure 48.

Corresponding test is realized for a laser repetition rate of 100Hz. In Figure 49 the results are shown. For 4 J/cm² few micro pits can be detected which occur in the beginning and do not grow within 10000 shots. This can be explained by the fact that a specific absorption limit is not reached so far. At a fluence of 4.8 J/cm² micro pits are formed in several steps but they do not grow together until 7000 pulses are reached. When the merging starts the damage grows much faster with increasing fluence. At 6.9 J/cm² a catastrophic damage is created. This test was stopped at a pulse number of around 2500. At 5.9 J/cm² micro pits are formed earlier than micro pits at 6.9 J/cm². This could be explained by the fact that creation of micro pits is not only dependent on laser parameters but also dependent on local material properties.

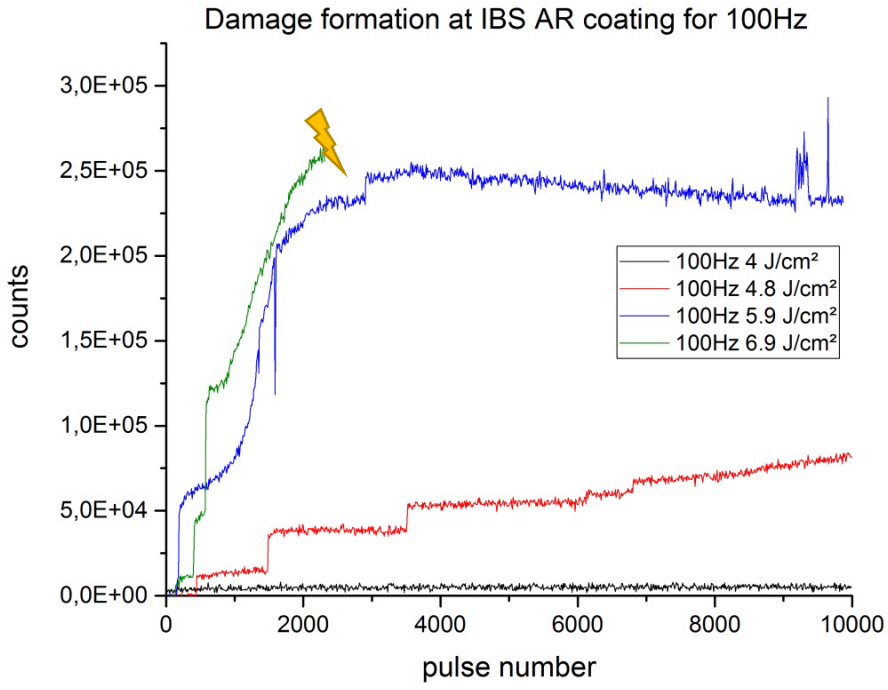

Figure 49: Damage formation at IBS AR coating for 100Hz laser rate; 10000 pulses, different fluences, flash symbolizes a catastrophic damage, background corrected counts on ordinate.

From these tests with different repetition rates it can be seen that final damage size and starting point of micro pit merging is dependent on fluence. Another point is that the process of merging happens much faster at 100Hz than at 20Hz.

Figure 50 shows LDM and Nomarski images for 100Hz tests.

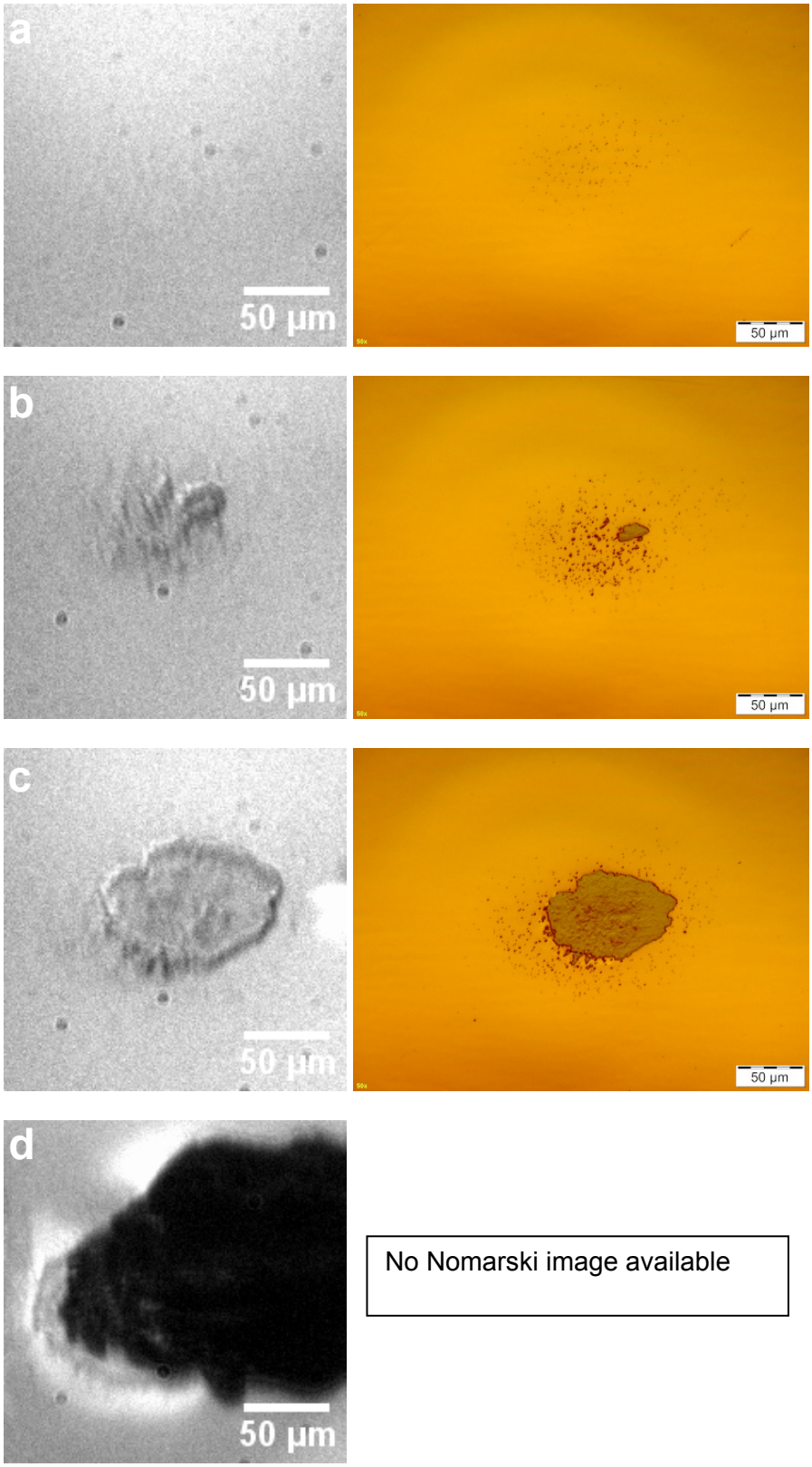

Figure 50: Comparison between LDM images (left) and Nomarski images (right) at different fluences for 100HZ tests: a) 4 J/cm² b) 4.8 J/cm² c) 5.9 J/cm² d) 6.9 J/cm².

Further tests with 20Hz and 100Hz are realized with identical fluences. First comparison is done with a fluence of 4.7 J/cm² and can be seen in Figure 51. The tests at 20Hz just create micro pits whereas at 100Hz micro pits grow together. The moment of micro pit creation looks quite random.

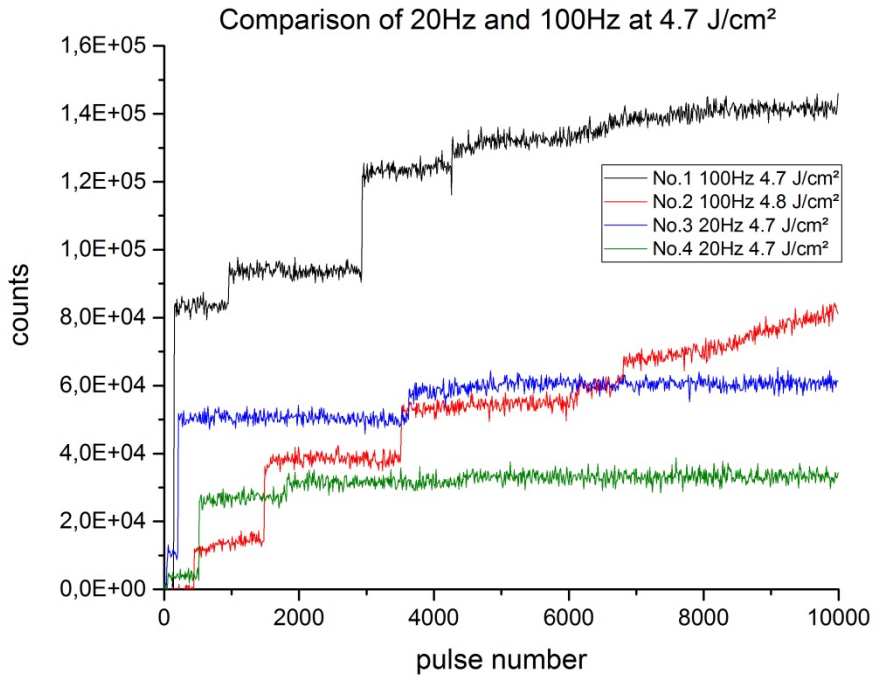

Figure 51: Comparison of damage formation for different laser repetition rates (20Hz and 100Hz) at 4.7 J/cm² and 10000 pulses, background corrected counts on ordinate.

The corresponding LDM images are displayed in Figure 52 - Figure 55. The figures show the images at positions of 2000, 4000, 6000 and 10000 pulses. This clarifies that at 20Hz only micro pits occur whereas at 100Hz the created micro pits grow together after specific number of pulses.

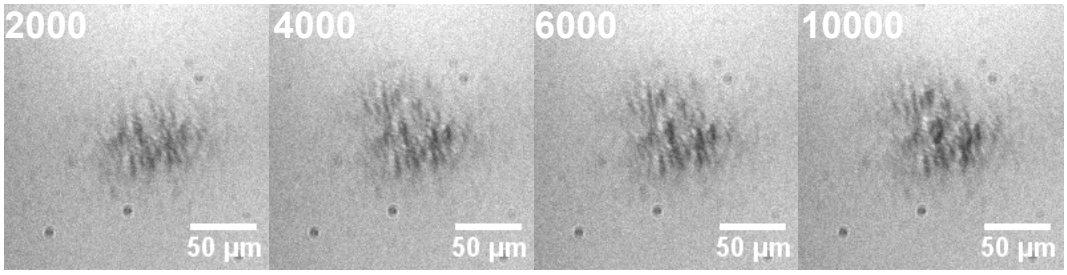

Figure 52: Damage formation AR IBS at 4.7 J/cm², 100Hz, No.1

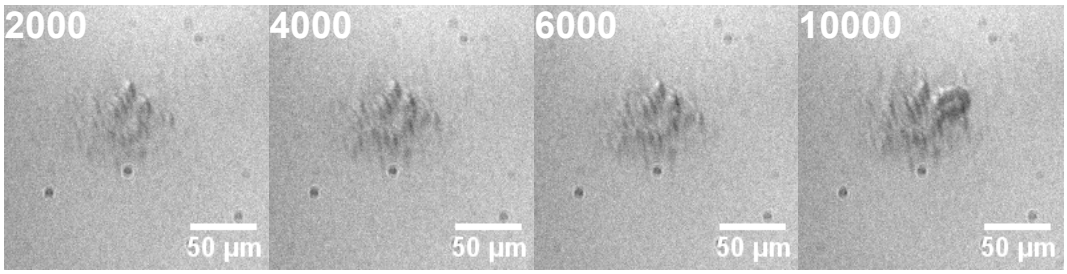

Figure 53: Damage formation AR IBS at 4.8 J/cm², 100Hz, No.2

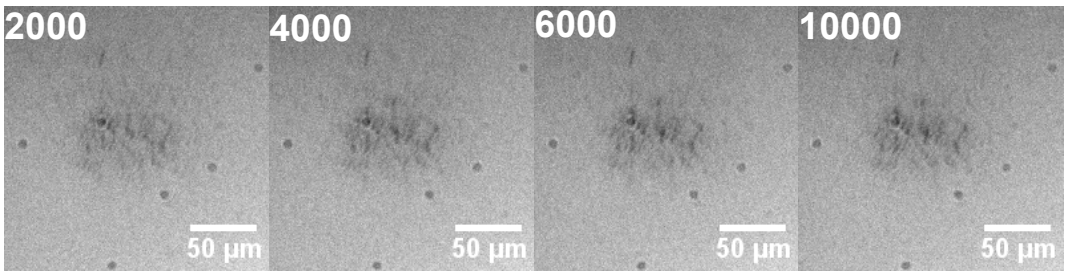

Figure 54: Damage formation AR IBS at 4.7 J/cm², 20Hz, No.3

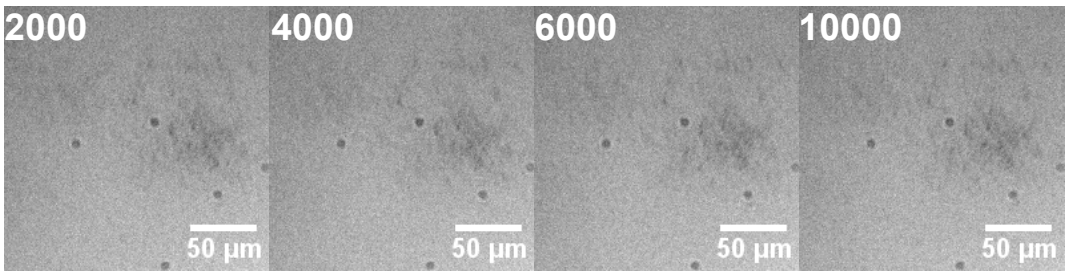

Figure 55: Damage formation AR IBS at 4.7 J/cm², 20Hz, No.4

Figure 56 shows results of corresponding test with a fluence of 5.4 J/cm². It can be seen that higher repetition rate of 100Hz generates damages and micro pits merging happens much earlier. At 20Hz one test show only micro pits whereat the second test show micro pit merging. The slope starts after 6000 pulses and is hence later than the starting point of micro pit merging at 100Hz.

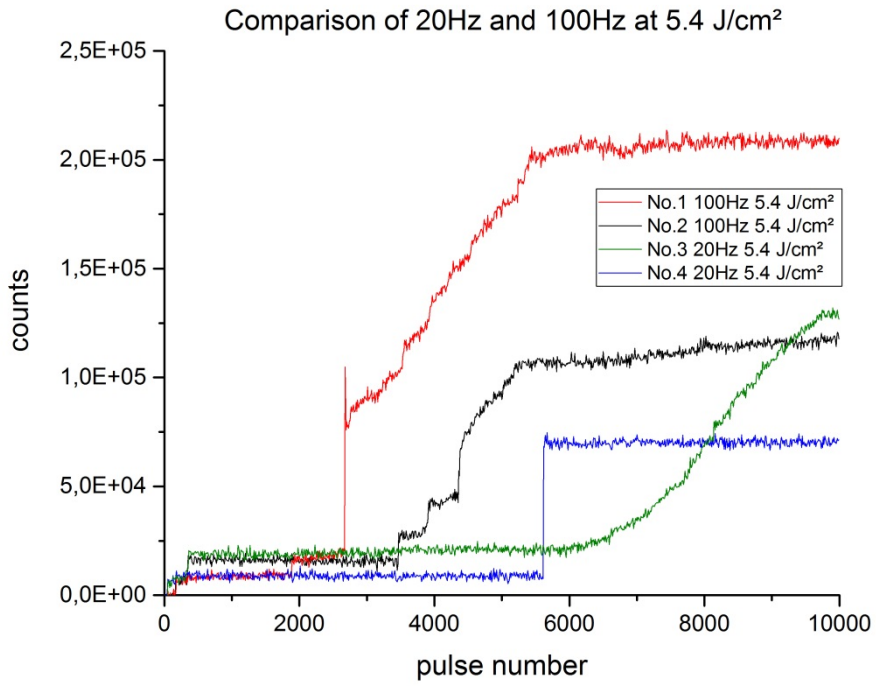

Figure 56: Comparison of damage formation for different laser repetition rates (20Hz and 100Hz) at 5.4 J/cm² and 10000 pulses, background corrected counts on ordinate.

As in the upper comparison also formation for this example is displayed in Figure 57-Figure 60. With the help of these LDM images the specific pulse numbers can be allocated to an image for better visualization.

To sum up, the repetition rate has an effect on damage formation when micro pits occurred. At 100Hz micro pits merge faster than micro pits at 20Hz. Another point is that a test within a repetition rate shows the dependency on fluence quite good.

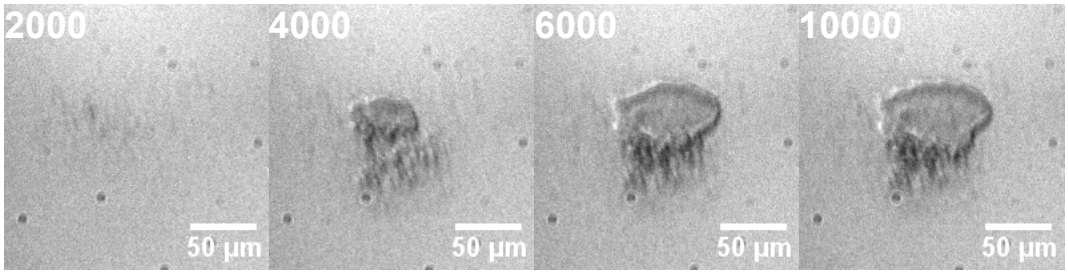

Figure 57: Damage formation AR IBS at 5.4 J/cm², 100Hz, No.1

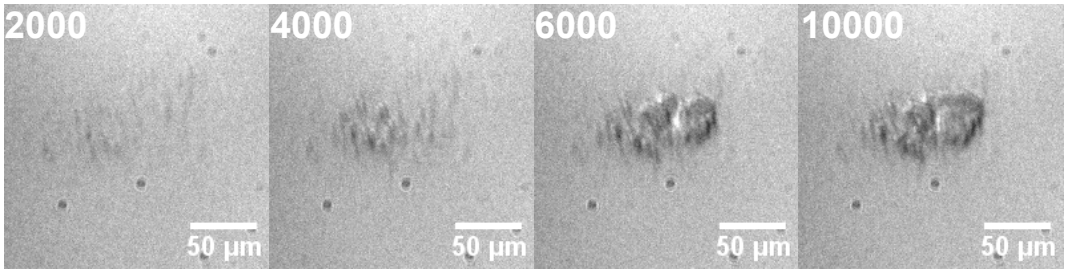

Figure 58: Damage formation AR IBS at 5.4 J/cm², 100Hz, No.2

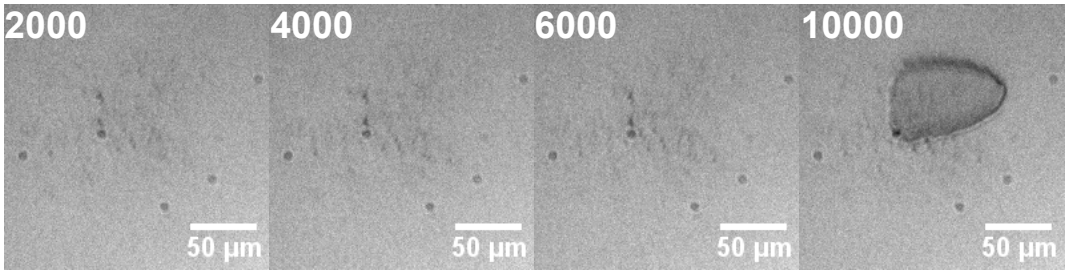

Figure 59: Damage formation AR IBS at 5.4 J/cm², 20Hz, No.3

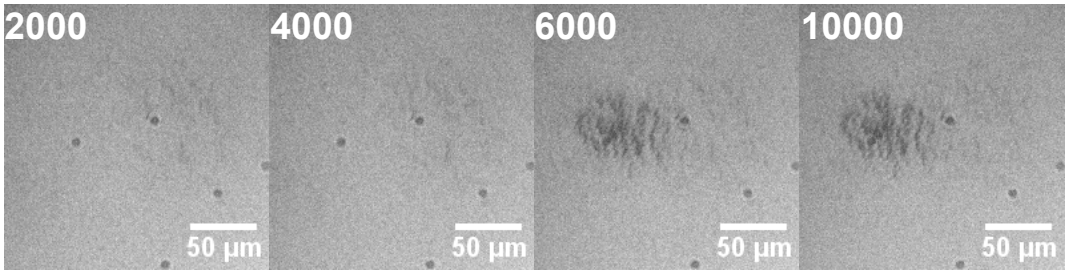

Figure 60: Damage formation AR IBS at 5.4 J/cm², 20Hz, No.4

5 Optimization of test bench

The experiments in chapter 4.2 and 4.3 are realized with the flash lamp Wallimex which is described in chapter 3.5.1. In the course of this work several disadvantages of flash lamp requires an optimization. The flash lamp and camera are triggered by laser output signal. These costs at least 14 ms at which the camera acquires but illumination do not work. To prevent this, a system is needed without trigger process. Next reason for optimization is the homogenous illumination of sample and the creation of high-contrast images.

Therefore a new type of illumination should be evaluated and integrated. First tests are realized with available light sources which are displayed with their parameters in Table 6.

Table 6: List of investigated light sources for optimization

	Osram Halogen Lamp Halopar 30	**Wallimex Flash Lamp Pro VE-200**	**Pearl LED Lamp**
Type of lamps	cw (670 lm)	Flashes (up to 200 Ws)	cw
Power	75 W	150 W	10 W
Color temperature	2900 K	5600 K	-

For comparison a small damage on AR coating with a size in the range of nearly 100 µm is created and an image is acquired with each type of illumination source. The results are displayed in Figure 61. Flash lamp and Halogen lamp are positioned at the port of vacuum chamber and illuminate sample inclined whereas the LED lamp is coupled at a second eye piece of LDM. The light is coupled over beam splitter and illuminates the sample without an angle.

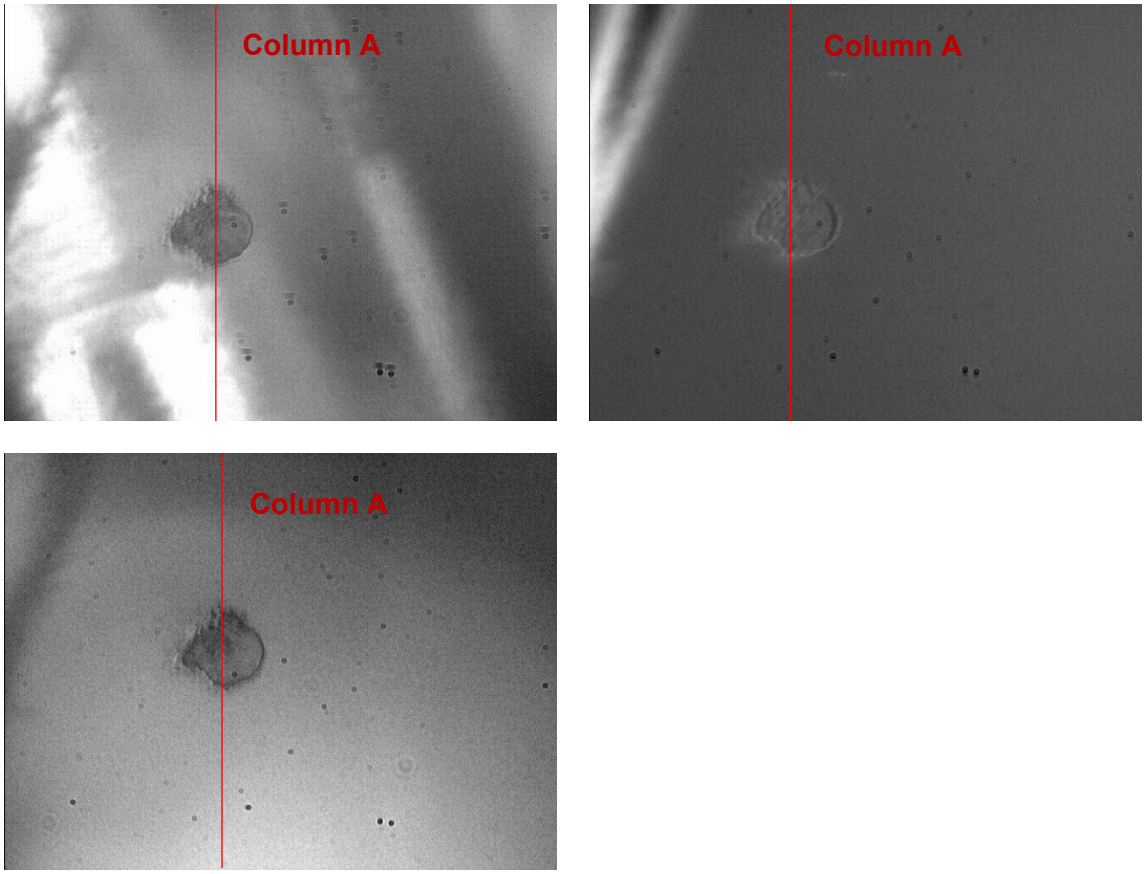

Figure 61: Damage on AR coating illuminated with different types of light sources, Halogen lamp (upper left), Flash light (upper right), LED lamp (lower left), red line marks the column A which is evaluated.

Just by consideration of upper figures it can be seen that images illuminated by Halogen lamp are too bright and images illuminated by flash lamp are in this case darker. This could be corrected with higher light exposure of the flash lamp. But this results in longer exposure time of camera which is unwanted. The homogeneity is best with the flash lamp but the contrast is rather low. The homogeneity with halogen lamp is extremely bad but contrast is even higher. The best compromise is given with the LED lamp. The contrast is pretty good and the homogeneity is in an acceptable range (see Figure 62).

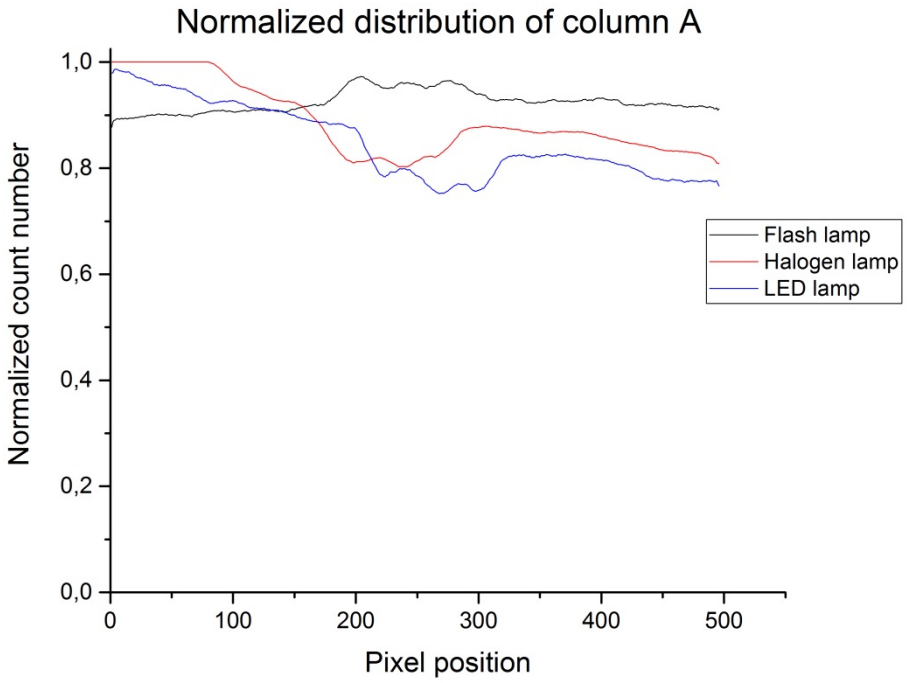

Figure 62: Normalized distribution of column A.

6 Summary

The setup of test bench is completed and successfully tested. It was shown that long distance microscopy is a powerful method for online investigation of damage formation and superior to conventional scattered light method. Small single damages with dimensions down to 3 µm can be resolved and for low repetition rates (1-20Hz), the damage formation can be visualized after each pulse.

Comparative tests with high reflective coatings confirmed that LIDT for IBS coatings is considerably higher than for EBE coated samples. It as shown, that the different coating types have different damage formation characteristics. Another important fact is that damage formation of both coatings has a point at a certain pulse number at which the slope is changed. This can be explained by the fact that damages do not grow further when they reached dimensions of beam diameter. The comparison between antireflective and high reflective IBS coatings shows that formation of damage at AR samples always starts with occurrence of micro pits. The completely different characteristic makes the comparison between HR and AR samples possible.

In a further step the characteristics of micro pits are investigated. Therefore created micro pits are investigated with LDM, Nomarski, WLIM and AFM. LDM and Nomarski show that micro pits can be resolved pretty well with LDM after optimization of illumination. The Nomarski microscope also shows that micro pit dimension is in a range lower than 10 µm. Furthermore micro pits appear not as single micro pits but many micro pits within the laser spot. WLIM and AFM confirm that micro pits are holes in the coatings. The dimensions which are measured are in the range of 1-4 µm for diameter of a single micro pit with depths in the range of 50-400 nm. This means that micro pits occur not only in the first layer but also in next coating layers. The damage formation for those coatings can be displayed over intensity distribution of each image which is measured in counts. This means that the values of each pixel in a region of interest are added up and allocate a value to each single image. The curve which is calculated out of these values characterizes the damage formation. This curve show steps when micro pits occur and a slope when these micro pits grow together. Due to the fact that micro pits occur with a single pulse there is the assumption that micro absorber in the coating layers are heated by laser beam until they reach a specific limit and create micro pits. By increasing fluence

those micro pits start to grow together when a threshold is reached. Some tests also show that micro pits do not grow together within 10k shots when this limit is not reached.

Last experiment investigates the influence of laser repetition rate on the LIDT. Therefore tests with 20Hz and 100Hz are realized. For a single laser rate several fluences are investigated and compared to each other. For both rates the trend can be seen that with higher fluences the merging starts earlier and final damage become larger. Also the slope when micro pits grow together becomes steeper by increasing fluences. Comparing both laser rates at same fluences it can be shown that micro pits with 100Hz grow faster than micro pits at 20Hz.

All in all the LDM is a good method for the online investigation of micro pits during laser induced damaging tests. Also the calculated curves from the acquired images can be used for characterizing the process of damage formation.

Some of the test results described above suffers from poor pulse to pulse stability of the laser system. Further tests should be performed with an improved system.

Most erroneous component of system is the laser itself. Not only pulse to pulse stability is higher than expected but also the spatial profile is changed by change the laser repetition rate. By changing a parameter like laser spot position on sample by beam guiding mirror all other components like LDM position, LDM focus and energy measurement need to adjust as well. This is quite time-consuming and demand setup on optimization.

7 Outlook

The setup need to be optimized. The illumination with LED can be developed and pulsed LED systems can be tested to improve the image quality. Furthermore the temporal resolution of 10 pulses with laser rates of 20Hz and 100Hz can be improved to get an image after each pulse also for these repetition rates.

For chapter 4.5 also 1Hz tests for total pulse numbers of 10000 were planned but due to problems in setup this is not realized so far. Based on results of already performed tests it is assumed that at samples, irradiated with 1Hz, micro pits merge even slower and later than micro pits at 20Hz and 100Hz.

Furthermore with existing setup the damage formation of different antireflective coatings can be investigated. It could be interesting if the formation of micro pits depends on layer material.

A next investigation could deal with the idea how exactly micro pits occur. This work shows only that micro pits occur with a single pulse and assume that micro absorber could be the reason for micro pit locations within the beam spot. Therefore the characteristic of layers have to be investigated before tests. This results can be compared to micro pit locations after tests.

Two completely different improvements deal with other online investigation methods. First a multi-channel plate (MCP) can be used to measure the ablated ions from layer's surface inside the vacuum chamber when micro pits or damages are created. Such MCP's for the use in a vacuum chamber are already available. With this method micro pits could be detected but images cannot be acquired with this method. Second idea deals with interferometry to detect the size and also the depth of micro pits and damages online.

Acquired LDM images are evaluated after tests. Next step could be the automation of online detection of micro pits. This means that the system evaluates micro pits during the test and give as output a background corrected image sequence and values for pulse numbers and fluences at which micro pits occur or grow together.

Table of figures

Table of tables

Table of equations

Bibliography

[1] C. H. T. E. Ronian Siew, "Laser Induced Damage Threshold of Optical Coatings," CVI Laser Optics, Albuquerque, 2013.

[2] Institute für Technische Physik, "www.dlr.de," DLR, [Online]. Available: http://www.dlr.de/tp/desktopdefault.aspx/tabid-10074/17193_read-41510/. [Accessed 3 7 2015].

[3] European Space Agency, "www.esa.int," 23 3 2012. [Online]. Available: http://www.esa.int/Our_Activities/Observing_the_Earth/The_Living_Planet_Programme/Earth_Explorers/ADM-Aeolus/Satellite. [Accessed 3 7 2015].

[4] European Space Agency, "www.esa.int," 17 1 2012. [Online]. Available: http://www.esa.int/Our_Activities/Observing_the_Earth/The_Living_Planet_Programme/Earth_Explorers/ADM-Aeolus/Overview. [Accessed 3 7 2015].

[5] Technical Committee ISO/TC 172 & CEN/TC 123, "ISO 21254 - Test methods for laser radiation induced damage threshold," International Organization for Standardization, Geneva, 2007.

[6] D. Ristau, Laser-Induced Damage in Optical Materials, Boca Raton, Florida: CRC Press Taylor & Francis Group, 2015.

[7] Lidaris LTD, "Laser Fluence, Intensity and Power," Lidaris LTD @ Vilnius University, 17 04 2015. [Online]. Available: http://lidaris.com/glossary-2/fluence/. [Accessed 17 04 2015].

[8] S. Martin, "FU Berlin," 12 2004. [Online]. Available: http://www.diss.fu-berlin.de/diss/servlets/MCRFileNodeServlet/FUDISS_derivate_000000001589/02_2-Grundlagen.pdf?hosts=. [Accessed 04 17 2015].

[9] P. Wagner, Laser-induced contamination on high-reflective optics, Stuttgart, 2014.

[10] K. Jousten, Wutz - Handbuch Vakuumtechnik - Theorie und Praxis, Wiesbaden: Vieweg & Sohn Verlag, 8.Auflage, 2004.

[11] Technical Committee, "ISO 3529/1 - Vacuum technology - Gerneral terms," 1981.

[12] Pfeiffer Vacuum GmbH, The Vacuum Technology Book Volume II - Know-how Book, Mainz: LOTS OF DOTS MediaGroup , 2013.

[13] Oerlikon leybold vacuum, Grundlagen der Vakuumtechnik, Köln, 2007.

[14] Arilou, "Wikipedia," 08 04 2015. [Online]. Available: http://de.wikipedia.org/wiki/Vakuum. [Accessed 21 04 2015].

[15] R.D.Sigler, Applied Optics - Family of Compact Schmidt-Cassegrain Telescope design, Washington D.C.: OSA Publishing, 1974.

[16] W.B.Wetherell and M.P.Rimmer, General Analysis of Aplanatic Cassegrain, Gregorian and Schwarzschild telescopes, Washington D.C.: OSA Publishing, 1972.

[17] R. Cox, A Cassegrain Maksutov Telesope for the amateur, S&T, 1957.

[18] J. Schönmuth, "Spezielle mikroskopische Methoden in den Geowissenschaften," Freiberg.

[19] S. E.Ruzin, "www.berkley.edu," Biological imaging Facility, 1999. [Online]. Available: http://microscopy.berkeley.edu/Resources/instruction/DIC.html. [Accessed 6 7 2015].

[20] GBS - Gesellschaft für Bild- und Signalverarbeitung mbH, "Neue Maßstäbe in der Weißlicht-Interferometrie," Ilmenau, 2008.

[21] TU Ilmenau - FG Graphische Datenverarbeitung, "www.tu-ilmenau.de," 7 6 2015. [Online]. Available: http://www.tu-ilmenau.de/gdv/forschung/projekte/3d-topographiemesstechnik-weisslichtinterferometrie/grundlagen-der-weisslichtinterferometrie/. [Accessed 6 7 2015].

[22] Veeco Instruments Inc., "Introduction to the NT9080 Surface Metrology System," Tucson, AZ, 2010.

[23] G. Binnig, C. Quate and c. Gerber, "Atomic Force Microscope," *Physical Review Letters 56,* pp. 930-933, 1986.

[24] DLR Institut für Technische Physik, *Rasterkraftmikroskopie,* Stuttgart: Poster.

[25] A. Kaless, "Grundlagen der optischen Entspiegelung," in *Dissertation - Oberflächenmodifizierung von Polymethylmethacrylat durch Plasmabehandlung*, Halle-Wittenberg, Martin-Luther-Universität, 2006, pp. 3-5.

[26] E. Hering and R. Martin, "Zweistrahlinterferenz," in *Photonik - Grundlagen, Technologie und Anwendungen*, Heidelberg, Springer Verlag, 2006, pp. 36-28.

[27] G. Litfin, "Reflexion," in *Technische Optik in der Praxis*, Heidelberg, Springer Verlag, 2005, pp. 61-64.

[28] Laseroptik GmbH, "Production methods - Ion Beam Sputtering," in *Laseroptik - Catalog 2015*, Garbsen, 2015, p. 27.

[29] T. Turner and R. Kirschner, "Thin film coatings," [Online]. Available: http://www.photonics.com/EDU/Handbook.aspx?AID=42399. [Accessed 03 08 2015].

[30] D. Ristau and T. Groß, "Ion Beam Sputter Coatings for Laser Technology," Proceedings of the SPIE 5963, Hannover, 2005.

[31] P. W. Baumeister, "Ion beam sputtering as method of depositing coatings," in *Optical Coating Technology*, Bellingham, SPIE, 2004, pp. 9-17.

[32] J. Groves, H. Wadley, A. Ritenour, D. Hass and R. Ratnaparkhi, "Electron Beam Directed Vapor Deposition," University of Virginia - Materials Science and Engineering Department, Charlottesville, VA.

[33] Coherent Laser Group, "Operators' s Manual - The Coherent Infinity - Nd:YAG Laser System," Santa Clara, 1998.

[34] Continuum, "BAP Tripler Setup for ETSC," San Jose, 2004.

[35] W. Riede, P. Allenspacher, L. Jensen and M. Jupe, "Analysis of the air-vacuum effect in dielectric coatings," DLR , Stuttgart, 2008.

[36] Oerlikon Leybold Vacuum GmbH, "Technische Daten SCROLLVAC SC 15 D," [Online]. Available: https://leyboldproducts.oerlikon.com/produkte/produktkatalog_04.aspx?cid=1599#Charcteristics. [Accessed 24 04 2015].

[37] Pfeiffer Vacuum GmbH, The Vacuum Technology Book Volume I, Asslar, 2008.

[38] Questar Corporation, "QM100 Long-Distance Microscope - Data Sheet," New Hope.

[39] D. B. Murphy, E. D. Salmon, K. R. Spring, M. Abramowitz and M. W. Davidson, "Olympus Microscopy Resource Center," Olympus, 2012. [Online]. Available: http://www.olympusmicro.com/primer/techniques/dic/dicintro.html. [Accessed 14 07 2015].

[40] P. Allenspacher, A. Ciapponi and W. Riede, "ALADIN Laser Optics Mitigation test: LO HR355 IBS," DLR , Stuttgart, 2012.

[41] W. Riede and P. Allenspacher, "Technical note on error analysis for laser damage tests," DLR, Institut of Technical Physics, Stuttgart, 2008.

[42] P. Allenspacher, A. Ciapponi and W. Riede, "ALADIN Laser Optics Mitigation test: LO AR355 IBS," DLR, Stuttgart, 2012.

[43] Paul Scherer Institut, Villingen, CH, 2015.

Appendix

List of performed tests

Table 7: List of performed tests

Test #	Internal sample #	Coating type	Coating process	Fluence [J/cm²]	Laser repetition rate [Hz]	Total number of pulses	Purpose, Annotation
1	1274	HR 355nm/45°	IBS	8.0	1	1	Single shot tests
2	1274	HR 355nm/45°	IBS	9.0	1	1	Single shot tests
3	1274	HR 355nm/45°	IBS	11.0	1	1	Single shot tests
4	1274	HR 355nm/45°	IBS	12.0	1	1	Single shot tests
5	1274	HR 355nm/45°	IBS	12.0	1	1	Single shot tests
6	1275	AR 355nm/0°	IBS	2.0	1	1	Single shot tests
7	1275	AR 355nm/0°	IBS	3.0	1	1	Single shot tests
8	1275	AR 355nm/0°	IBS	4.0	1	1	Single shot tests
9	1275	AR 355nm/0°	IBS	13.0	1	1	Single shot tests
10	1274	HR 355nm/45°	IBS	7.0	1	50	Example for damage formation characteristic
11	1274	HR 355nm/45°	IBS	6.2	1	100	Multi shot tests
12	1274	HR 355nm/45°	IBS	6.5	1	100	Multi shot tests
13	1274	HR 355nm/45°	IBS	6.6	1	100	Multi shot tests
14	1274	HR 355nm/45°	IBS	7.1	1	100	Multi shot tests
15	1205	HR 355nm/45°	EBE	3.4	1	100	Multi shot tests
16	1205	HR 355nm/45°	EBE	3.6	1	100	Multi shot tests

17	1205	HR 355nm/45°	EBE	3.6	1	100	Multi shot tests
18	1205	HR 355nm/45°	EBE	3.8	1	100	Multi shot tests
19	1205	HR 355nm/45°	EBE	3.8	1	100	Multi shot tests
20	1275	AR 355nm/0°	IBS	1.9	1	100	Multi shot tests
21	1275	AR 355nm/0°	IBS	3.3	1	100	Multi shot tests
22	1275	AR 355nm/0°	IBS	4.0	1	100	Multi shot tests
23	1276	AR 355nm/0°	IBS	-	100	-	Investigation of micro pits
24	1280	AR 355nm/0°	IBS	5.5	100	10000	Investigation of laser repetition rate
25	1280	AR 355nm/0°	IBS	4.7	20	10000	Investigation of laser repetition rate
26	1280	AR 355nm/0°	IBS	5.4	20	10000	Investigation of laser repetition rate
27	1280	AR 355nm/0°	IBS	6.2	20	10000	Investigation of laser repetition rate
28	1280	AR 355nm/0°	IBS	4.0	100	10000	Investigation of laser repetition rate
29	1280	AR 355nm/0°	IBS	4.8	100	10000	Investigation of laser repetition rate
30	1280	AR 355nm/0°	IBS	5.9	100	10000	Investigation of laser repetition rate
31	1280	AR 355nm/0°	IBS	6.9	100	10000	Investigation of laser repetition rate
32	1280	AR 355nm/0°	IBS	4.7	20	10000	Investigation of laser repetition rate
33	1280	AR 355nm/0°	IBS	4.7	100	10000	Investigation of laser repetition rate
34	1280	AR 355nm/0°	IBS	5.4	20	10000	Investigation of laser repetition rate

35	1280	AR 355nm/0°	IBS	5.4	100	10000	Investigation of laser repetition rate
36	1280	AR 355nm/0°	IBS	5.4	100	10000	Investigation of laser repetition rate

Energy Calibration

Before LIDT tests starts, a calibration is needed. Therefore a powermeter in sample position and an energy detector behind a wedge is set up. The energy detector is then calibrated with the help of power meter.

This calibration is realized before each test. The calibration of 20Hz and 100Hz are in same range but 1Hz calibration differs a lot. This can be explained with the fact that between these two measurements the setup is optimized and the beam which hits the energy detector at 20Hz and 100Hz tests is split after wedge again with a beamsplitter.

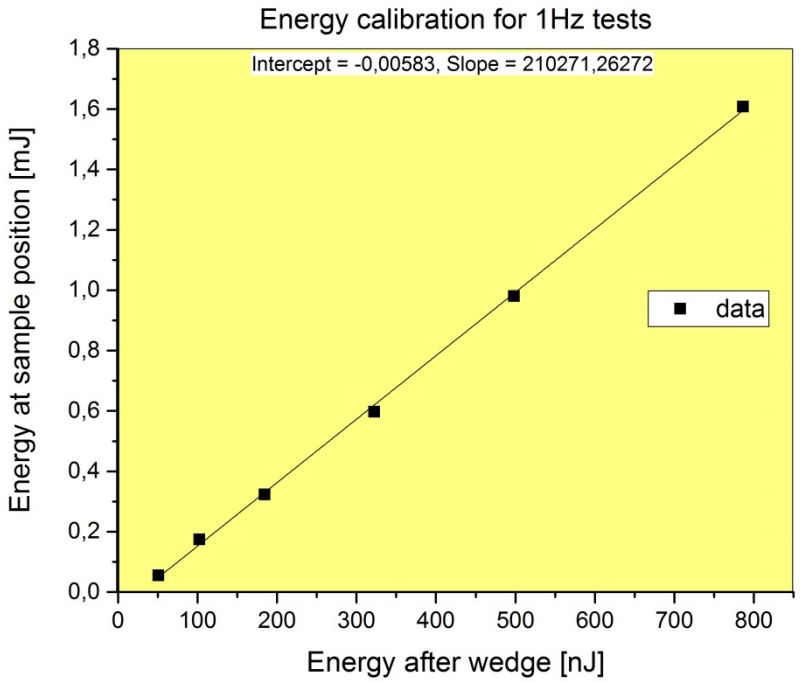

Figure 63: Energy calibration for 1Hz tests

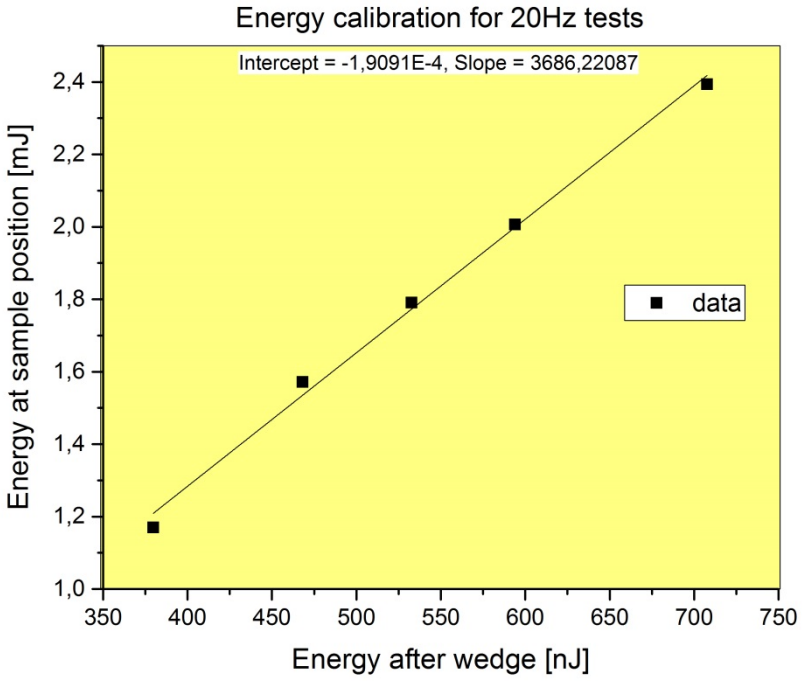

Figure 64: Energy calibration for 20Hz tests

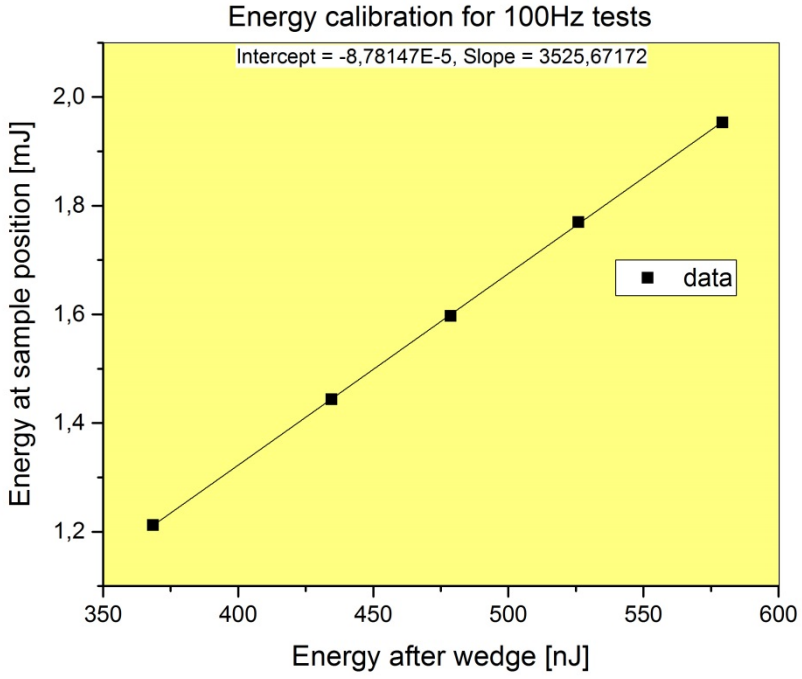

Figure 65: Energy calibration for 100Hz tests

Programming code of Andor software to extract image sequence into single images

```
//Program to extract sif image sequence into single background corrected images with tif format

Max = 50              //Total number of images

Root$ = "G:\AOS\5_Mitarbeiter\Mucha\Masterthesis\01_Versuchsdaten\01_Bilder\04_Versuch_IBS_Damage_Entstehung_1274\35_8\35_LDM_MM_Mon_Jun_8_2015_8"
        //data path

load(#2001, "G:\AOS\5_Mitarbeiter\Mucha\Masterthesis\01_Versuchsdaten\01_Bilder\13_Versuch_150722_IBS_AR_reprate_1279\Daten_100Hz\26\150722_1279_background_27.sif")
        //load background image into window 2001

load(#2000,Root$;".sif")            //load sif file into a new window

minimizewindow(#2000)

for i = 1 to Max step 1             //for loop

        #i = #2000{i} [1<<658,1<<496]        //extract each image of sequence

        #j= #i-#2001                //subtract background image from single image

        ExportTiff(#j,Root$;"_";str$(i);".tif",1,1)  //save corrected image as tif image

        closeWindow(#i)

next

closewindow (#j)

closewindow(#2000)

closewindow(#2001)
```

Programming Code of Mathematica 10.0

```
(*Mathematica Code for background correction if it is not already done by Andor software.
Then counting total counts in defined ROI and display them as function of pulse number*)

a=Import["G:\\AOS\\5_Mitarbeiter\\Mucha\\Masterthesis\\01_Versuchsdaten\
\01_Bilder\\14\\44\\150727_1279_44_900.tif","RawData"];

top=100;
bottom=300;
left=300;
right=500;
roi=a[[top;;bottom, left;;right]];

MatrixPlot@a
MatrixPlot[roi, ColorFunction->GrayLevel]
```

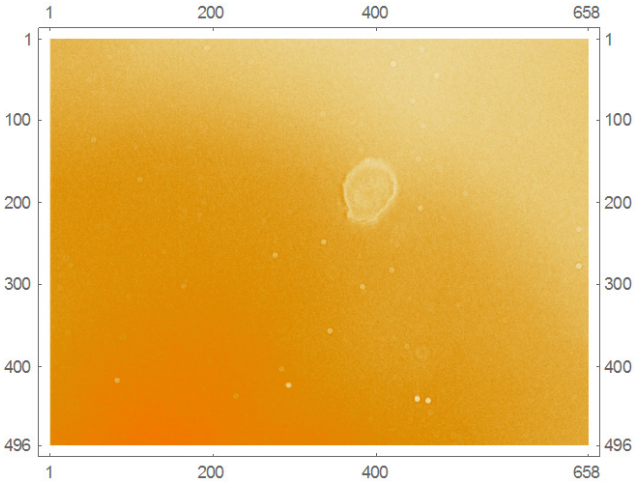

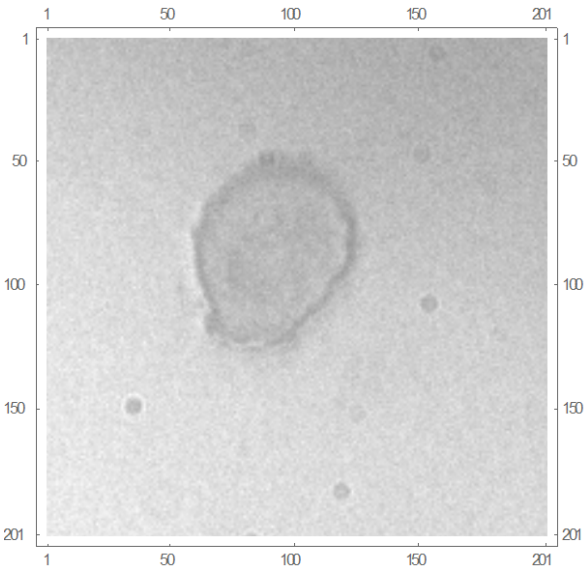

```
totalcounts={};

Do[
img=Import["G:\\AOS\\5_Mitarbeiter\\Mucha\\Masterthesis\\01_Versuchsdaten\\01_Bilder\\14\\44\\150727_1279_44_"<>ToString[i]<>".tif","RawData"];

background=Import["G:\\AOS\\5_Mitarbeiter\\Mucha\\Masterthesis\\01_Versuchsdaten\\01_Bilder\\14\\44\\150727_1279_background_44_1.tif","RawData"];

  roiimg=img[[top;;bottom,left;;right]];

  roiback=background[[top;;bottom,left;;right]];
  roiimgcorr=Abs[roiimg-roiback];

  countnmb=Total[roiimgcorr,2];

  AppendTo[totalcounts,countnmb];

  ,{i,1,1000,1}];

Length@totalcounts

graphiclistplot=ListLinePlot[MovingAverage[(totalcounts/(Max@totalcounts)),10],FrameLabel→{"Tot.Counts","Pulse Number"},PlotLabel→"150727_1279_44"
```

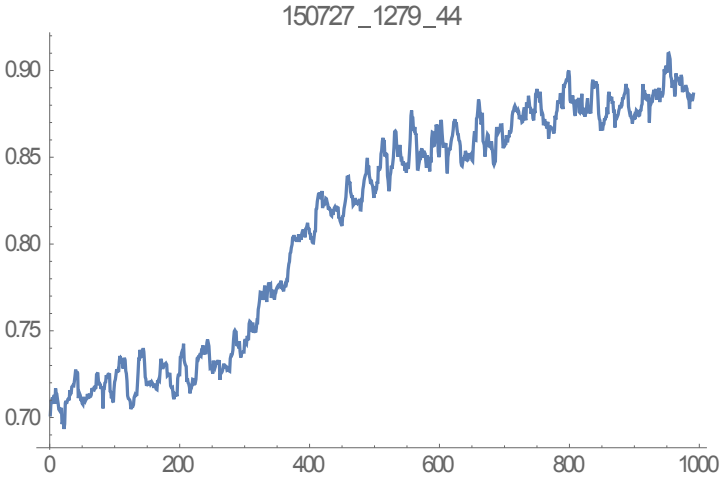


```
Export["G:\\AOS\\5_Mitarbeiter\\Mucha\\Masterthesis\\03_auswertung\\Mathematica\\150727_1279_44.tif",graphiclistplot,ImageResolution->140];

Export["G:\\AOS\\5_Mitarbeiter\\Mucha\\Masterthesis\\03_auswertung\\Mathematica\\150727_1279_44.csv",totalcounts];
```

Overview of vacuum ranges

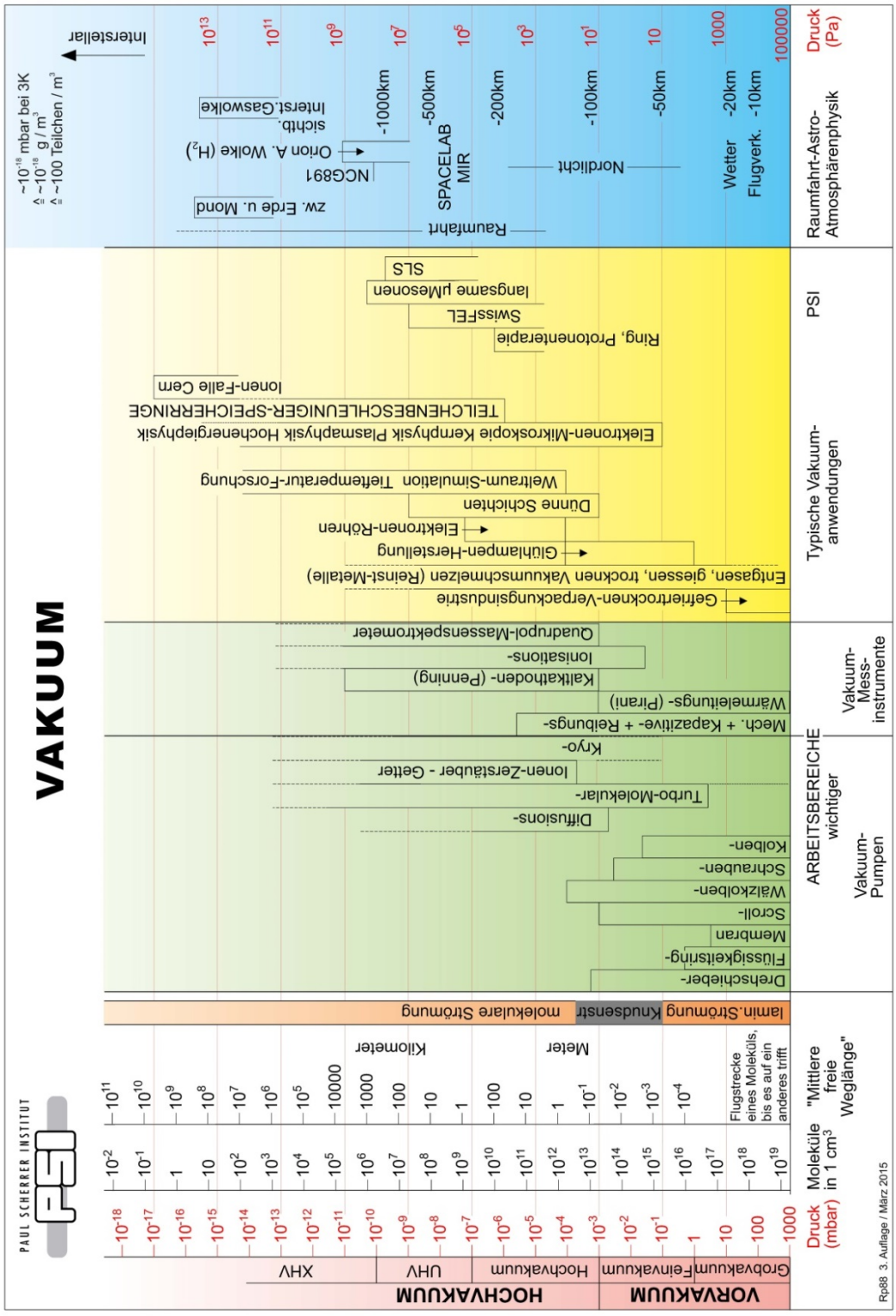

Figure 66: Overview of vacuum ranges [43]

Statement of affirmation

I hereby declare that the project thesis submitted was in all parts exclusively prepared on my own, and that other resources or other means (including electronic media and online sources), than those explicitly referred to, have not been utilized.

All implemented fragments of text, employed in a literal and/or analogous manner, have been marked as such.

Stuttgart, 21.08.2015

_____

Manuel Mucha